The effects of topography and soil properties on radiocesium concentrations in forest soils in Fukushima, Japan

Misa Yasumiishi[1], Taku Nishimura[2], Jared Aldstadt[1], Sean J. Bennett[1], Thomas Bittner[1]

[1]Department of Geography, State University of New York, the University at Buffalo

5 [2]Laboratory.of Soil Physics and Soil Hydrology, Graduate School of Agricultural and Life Sciences, The University of Tokyo

Correspondence to: Misa Yasumiishi (misayasu@buffalo.edu)

10

Abstract. This research collected forest soil samples in the summers of 2016, 2017, and 2018 from Fukushima, Japan, where the 2011 Fukushima Daiichi Nuclear Power Plant (FDNPP) accident contaminated the land. The purpose of this study was to examine how the local topography influenced the radiocesium (Cs-137) distribution patterns in soils over the years since the accident. As an analytical method, the generalized additive models (GAM) was used to determine at what percentages the topographic parameters explain Cs-137 contamination levels down to a depth of 30 cm. For comparison, topographic

15 parameters were extracted from both 1 m and 10 m digital evaluation models (DEMs). The effects of topography were compared with the effects of the soil water content and dry soil bulk density. An additional Tukey's honestly significant difference (HSD) test was conducted to determine the significance of the hillslope aspect and vegetation cover differences on concentration predictions. The results showed that, at this study site, topographic parameters extracted from the 10 m DEM

20 better predicted Cs-137 levels. The models with a single topographic parameter did not explain Cs-137 levels higher than 28.31 %. However, combining the parameters improved the explanation percentages. The relative influences of topographic parameters and soil properties were similar throughout the soil depth, showing their subsurface co-functionalities for Cs-137 concentration levels. Tukey's HSD test results showed the inter-effects of topography and vegetation cover differences. The results of this study indicate that the selection of topographic parameters, as well as the chosen methods of their extractions,

25 have implications for physical models assessing radionuclide contamination levels.

1 Background

Radionuclides released from atomic bomb explosions and nuclear accidents have become a research topic for two different purposes: (1) assessing radioactivity levels to protect humans from health risks (Davis, 2016, Fesenko, et al., 2007, Tsuda, 2015) and (2) modeling surface soil loss and yields using those radionuclides as environmental tracers (Bennett, et al., 2005, Loughran, et al., 1987, Lowrance, et al., 1988, Mabit, et al., 2007, Martz and De Jong, 1987, Pennock, et al., 1995, Quine, et al., 1997, Ritchie and Ritchie, 1995, Wallbrink, et al., 2002, Walling, et al., 2007, Xinbao, et al., 1990). One of the most commonly researched radionuclides is radiocesium (cesium-137; Cs-137). Cs-137 is a byproduct of nuclear fission, which is a mechanism for generating energy, and it does not naturally exist in the environment (Amaral, et al., 1998, IAEA, 2015, Tsoulfanidis, 2012). Atomic bomb explosions began emitting Cs-137 into the atmosphere in the late 1940s (Mahara, 1993), and emissions were highest from the late 1950s through the early 1960s, when atomic bomb testing was most active during the Cold War (Ritchie and McHenry, 1990, The Arms Control Association, 2019).

Cs-137 emits gamma-ray radiation, and this radiation can be harmful to organisms – including humans – when they are exposed to or inhale Cs-137 or intake Cs-137 via contaminated food or water at a high dosage (EPA, 2012, IAEA, 2019, Wrixon, 2004). The negative effects of radiation exposure on humans range from minor physiological symptoms to mortality (IAEA, 2001, IAEA, 2020, Scott, 2004). Biological consequences in plants and animals have been reported after the Chernobyl Nuclear Power Plant accident in 1986 (Barker, et al., 1996, Kovalchuk, et al., 2000, Møller and Mousseau, 2006).

Once released, Cs-137 may be dissolved in water (Iwagami, et al., 2015, Osawa, et al., 2018, Sakuma, et al., 2018, Tsuji, et al., 2016) or adsorbed into soil particles. Cs-137 is positively charged and has an affinity for clay minerals, which are negatively charged because of their ion composition in a crystal structure. Cs-137 can, thus, be fixed in clay mineral structures by exchanging positions with other positive elements, such as potassium or magnesium (Claverie, et al., 2019, Fan, et al., 2014, Murota, et al., 2016, Nagao, 2016, Nakao, et al., 2008, Ohnuki and Kozai, 2013, Park, et al., 2019, Ritchie and Ritchie, 1995).

When used as a tracer for geomorphological analysis, Cs-137 becomes a signal indicating where soils—particularly clay soils—accumulate or are lost. Whether Cs-137 moves by being dissolved in water or with soil particles, topography plays an important role in the process. It determines how precipitation flows on the ground surface and migrate subsurface and, hence, determines the directions of Cs-137's movement on the surface and its concentration levels in soils (Komissarov and Ogura, 2017, Martin, 2000, Roering, et al., 2001, Roering, et al., 1999, Schimmack, et al., 1994, Schimmack, et al., 1989, Teramage, et al., 2014).

In Fukushima, Japan, the Fukushima Daiichi Nuclear Power Plant (FDNPP) underwent hydrogen explosions in March 2011. The accident was caused by a power outage at the plant because, following a strong earthquake, a tsunami damaged the plant's

60 power generators (IAEA, 2015, Mahaffey, 2014). The environment in nearby towns was contaminated by the radioactive plume released from the plant. Since the accident, numerous field research activities have taken place in the region to assess contamination levels and devise remediation strategies. One particular interest among researchers has been examining the Cs-137 accumulation differences between Fukushima and the region affected by the Chernobyl Nuclear Power Plant (CNPP) accident in 1986. The CNPP and the FDNPP accidents are the only two nuclear power plant accidents categorized as Level 7

65 – the highest level on the International Nuclear and Radiological Event Scale (INES) (IAEA, 2015, IAEA and INES, 2008, Mahaffey, 2014). However, the climates and topographies of the Fukushima and Chernobyl regions differ (Table 1), and researchers have suspected that Cs-137 may behave differently in both areas.

Table 1. A snapshot of climates, topographies, and soil formations between the FDNPP accident–affected area and the CNPP
70 **accident–affected area.**

	FDNPP accident–affected area	CNPP accident–affected area
Climate	Cfa (humid climate; Köppen climate classification system).	Dfb (Warm-summer humid continental climate; Köppen climate classification system).
	Average annual precipitation: 1,361.6 mm (Japan Meteorological Agency, 2019).	Average annual precipitation: 621 mm (Climate-Data.Org, 2019).
Topography and vegetation cover	Mountainous. Forests are covered with deciduous and evergreen trees.	Steppes and plateaus.
Natural soil transformation	Volcanic activities and weathering, deposition.	Glacial activities and weathering, deposition.

1.1 Literature review and aims of this study

The authors reviewed 30 articles published after the FDNPP accident, all of which conducted soil sampling in the Fukushima region (Table 2). These articles described sampling timing and locations, land-use types, sample collection methods, and

75 sample depth.

A disparity identified in the literature review is that only a few research projects in the Fukushima region have incorporated topographic parameters, while some projects in Eastern Europe have addressed topographic parameters in Cs-137 accumulation patterns (Korobova, et al., 2010, Korobova, et al., 1998, Korobova and Romanov, 2009, Korobova and

80 Romanov, 2011, Korobova, et al., 2019, Korobova, et al., 2007, Linnik, et al., 2013, Linnik, et al., 2020, Linnik Vitaly, 2018, Vanden Berghe and Gulinck, 1987).

3

Past literature has pointed out the importance of topography for understanding physical processes, including Cs-137 behavior, in the environment. (Zaslavsky and Sinai, 1981) stated that topography was the controlling factor in the mechanism of soil water distribution in a catchment (as cited in (Moore, et al., 1988). (Moore, et al., 1988) found that the most effective topographic parameter to identify the surface gully erosion was $\ln(A_s$: the unit area divided by the slope). (Heimsath, et al., 1999) examined the relationships among cosmogenic nuclides, topography (curvature), and soil depth. They concluded that the variable thickness of soil that we observe is a function of topographic curvature.

Based on this background and literature review, the current study examined how well topographic parameters explain and predict Cs-137 concentration levels. Since about 70 % of the Fukushima region is forested (Japan Forest Agency, 2017), this study used forest soils as a research subject. For analysis, four steps were incorporated.

    1) Test 1: Conducting a descriptive analysis of Cs-137 concentration patterns on a simple, representative hillslope.

    2) Test 2: Examining the explanation power of multiple topographic parameters on Cs-137 accumulation levels.

    3) Test 3: Examining the effect of vegetation cover and locational grouping on Cs-137 level predictions if Test 2 did not return significant results.

    4) Test 4: Examining the applicability of the results of Test 2 in a basin-wide spatial Cs-137 prediction.

This case study sought to provide a further understanding of Cs-137's behavior in forest soils and to contribute to future response and remediation strategies for radioactive contamination.

Table 2. Soil sampling projects conducted in the Fukushima region following the 2011 FDNPP accident.

Article #	Authors	Publication year	Sampling year	Land use type	Soil collection methods	Deepest sample depth	Reporting unit	Topographic parameters
1	Shiozawa et al.	2011	2011	Rice paddies	Scoop and cylinder	15 cm	Bq kg^{-1} Bq m^{-2}	N/A
2	Tagami et al.	2011	2011	Flower garden	Scoop	12 cm	Bq kg^{-1}	N/A
3	Tanaka et al.	2012	2011	Field, orchard	Stainless steel pipe	30 cm	Bq kg^{-1} Bq m^{-2}	N/A
4	Fujiwara et al.	2012	2011	Forest, rice paddy, urban	House-made soil sampler	30 cm	Bq kg^{-1} Bq m^{-2}	N/A
5	Koarashi et al.	2012	2011	Croplands, grasslands, pastures	Core sampler	20 cm	Bq kg^{-1} Bq m^{-2}	Altitude
6	Kato et al.	2012	2011	Home garden at a residence	Scraper plate	30 cm	Bq kg^{-1} Bg m^{-2}	N/A
7	Ohno et al.	2012	2011	Wheat fields, rice paddies, orchards, and forestland	A stainless steel core sampler	20 cm	Bq kg^{-1} Bq m^{-2}	N/A
8	Endo et al.	2012	2011	Uncultivated lands, such as	N/A	10 cm	Bq g^{-1} Bq m^{-2}	N/A

				shrubs, school playgrounds, flowerbeds, and a sandbox (in a park)				
9	Yamamoto et al.	2012	2011	Roadside, school playgrounds and paddy or dry fields	Stainless steel pipe, soil sampler	30 cm	Bq kg^{-1} Bq m^{-2}	N/A
10	Taira et al.	2012	2011	Undisturbed surface soils	Core sampling	10 cm	Bq kg^{-1} Bq m^{-2}	N/A
11	Zheng et al.	2012	2011	Research center ground, public park, garden, forest	N/A	13 cm	mBq g^{-1}	N/A
12	Endo et al.	2013	2011	Rice paddies, uncultivated land	N/A	30 cm	Bq g^{-1} Bq m^{-2}	N/A
13	Nakanishi et al.	2013	2011	General farming field, vegetable field, wheat field, paddy soil field for rice	N/A	N/A	Bq kg^{-1}	N/A
14	Matsunaga et al.	2013	2011	Croplands, grasslands, forests	Core sampler	25 cm	Bq m^{-2}	N/A
15	Tanaka et al.	2013	2012	Paddy field	Plastic corer, stainless steel pipe equipped with an inner plastic corer	30 cm	Bq g^{-1} Bq m^{-2}	N/A
16	Saito et al.	2014	2011	N/A	House-made soil sampler	5 cm	Bq m^{-2}	N/A
17	Takata et al.	2014	2011–2012	Upland, paddy fields, orchard, meadow	Hand sampler	15 cm	Bq kg^{-1}	N/A
18	Sakai et al.	2014	2011–2012	Rice paddies	Core sampler	20 cm	Bq kg^{-1}	N/A
19	Nakanishi et al.	2014	2011–2012	Forest	N/A	10 cm	Bq kg^{-1} Bq m-2	N/A
20	Fujii et al.	2014	2011–2012	Forest	Core sampler	20 cm	Bq kg^{-1} Bq m^{-2}	N/A
21	Yoshikawa et al.	2014	2012	Paddy field	Soil sampler	15 cm	Bq kg^{-1}	N/A

| 22	Takahashi et al.	2015	2011–2012	Forests, pasture, meadow, farmland, tobacco field, rice paddy	Scraper plate	10 cm	Bq kg^{-1} Bq m^{-2}	Altitude
23	Maekawa et al.	2015	2011–2012	N/A	Stainless steel tube	15 cm	Bq kg^{-1} Bq m^{-2}	N/A
24	Matsuda et al.	2015	2011–2012	N/A	Scraper plate	8 cm	Bq kg^{-1} Bq m^{-2}	N/A
25	Saito et al.	2015	2011	Fields with little vegetation (farm fields were avoided)	Referred to (Onda, et al., 2015)	5 cm	Bq m^{-2}	N/A
26	Lepage et al.	2015	2013	Paddy fields	Augur	20 cm	Bq kg^{-1} Bq m^{-2}	N/A
27	Onda et al.	2015	2011	Forest floor, grassland, and paddy field	Plastic container, core sampler	5 cm	Bq kg^{-1} Bq m^{-2}	N/A
28	Yang et al.	2016	2011–2014	Rice paddies	Referred to (Onda, et al., 2015)	30 cm	Bq kg^{-1} Bq m^{-2}	N/A
29	Ayabe et al.	2017	2013–2015	Secondary forests	N/A	5 cm	Bq kg^{-1} Bq m^{-2}	N/A
30	Wakai et al.	2019	2014	Roadside, paddy, upland, canal ditch, mountain	Soil sampling scoop	5 cm	Bq kg^{-1}	N/A

2 Study site description

2.1 Topography

105 The soil sampling site was in a forest in Iitate Village, Fukushima, Japan, which is located about 35 km northwest of the FDNPP (Fig. 1). Hydrogen explosions at the FDNPP occurred multiple times, and the radioactive plume was carried in different directions and at various distances with the wind (Hashimoto, et al., 2012, IAEA, 2015, MEXT, 2011). Figure 2 shows the timing and main locations of the Cs-137 fallout (IAEA, 2015). The study site was under the plume released on 15 March 2011 from FDNPP Unit 2. The plume initially moved toward the southwest and then, following a change in wind

110 direction, toward the northwest, resulting in wet deposition across northwestern Fukushima and other prefectures (IAEA, 2015).
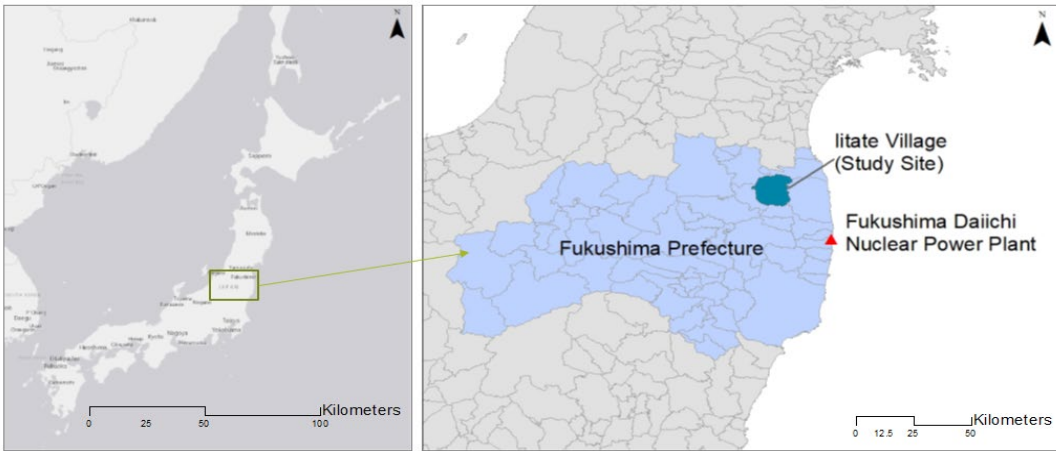
Figure 1. Locations of the FDNPP and the study site (Basemap: ESRI, HERE, Garmin, © OpenStreetMap contributors. Distributed under a Creative Commons BY-SA License.; Iitate Village, Fukushima, Japan (Japan municipal border map: © ESRI Japan).
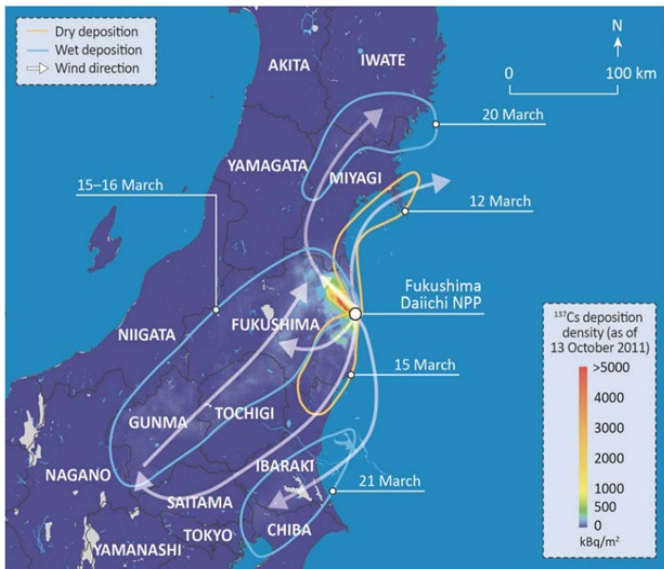
115

Figure 2. Timing and locations of the main Cs-137 deposition events following the explosions at the FDNPP (Map: IAEA [2015]).

When driving into the study site region, visitors see hills and mountains covered with forests. Winding, narrow roads connect the town center, residential areas, and farmlands scattered across the lowlands (Fig. 3). The geology of the Fukushima region

120 is mostly composed of Paleozoic metamorphic rocks and Paleo-Mesozoic igneous rocks (Forest Management Center, 2017). The mountains in the region are low-rising mountains with micro-topographies, where narrow – and sometimes steep – streams cut through the hillslopes.

Figure 3. An aerial views of the study site, facing northwest. The image shows the road stretching toward the village center (shot in 2018).

These mountains are covered in deciduous and conifer trees, and litter accumulates on the forest floor. During spring and summer, canopies cover the hills and the sky is typically not visible from the ground. However, at the particular study site in this research, the canopies are not thick at the tops of the hills. Standing on the highest ridge, hikers have a view of nearby mountains rolling toward the southeast.

These forests are not all "natural" or "native." The Japanese government began tree-planting and land management projects in the late seventeenth century to mitigate the overharvesting of lumber and land degradation due to the country's increasing population.

The most recent planting records by the Ministry of Agriculture and Fisheries were found in the forest. They showed that on the west side hills of the basin, 6,300 Japanese cypress (*Chamaecyparis obtuse)* saplings were planted in May 1998. On the east side hills of the basin, 74,100 red pine (*Pinus resinosa*) saplings were planted in April 1965. The spatial boundaries of the planning areas were not clear.

Whether the land-use history of the forests affects radionuclide behavior is an important question. However, since the radionuclide fallout happened recently, and since no major forestry work (e.g., new planting) has been conducted in the area after the accident, land-use history was not considered in the following analysis.

2.2 Background contamination levels

Understanding Cs-137 contamination requires the determination of background contamination levels. Background Cs-137 contamination data before the FDNPP accident were unavailable for the forests sampled in this study. According to previous

8

literature, in Japan, Cs-137 levels have varied from 15 Bq kg^{-1} or lower to 100 Bq kg^{-1}, although the 100 Bq kg^{-1} measurement was an outlier (Table 3). Conservatively, 100 Bq kg^{-1} was used as the background contamination level in the following analysis.

150 **Table 3. Background levels of Cs-137 in soils in Japan before the FDNPP accident (the highest concentration at a measured soil depth).**

Location and approx. distance from FDNPP	Sample year	Highest concentration (approx.)	Measured depth (approx.)
Ibaragi (180 km southwest of FDNPP; Yamaguchi, et al., 2012)	1996	50 Bq kg^{-1} (forest)	10 cm
Sea of Japan side (Komamura, et al., 2006)	1959–1978	100 Bq kg^{-1} (rice paddy)	NA
Aomori (350 km north of Fukushima; (Tsukada, et al., 2002)	1996-1997	15 Bq kg^{-1} (paddy soil)	5–20 cm
Fukushima City, Fukushima (60 km northwest of Fukushima;(MEXT, 2006)	2005	21 Bq kg^{-1}	0–5 cm

3 Soil sampling

3.1 Field sampling

155 Soil samples were collected in 2016, 2017, and 2018 during summer (Fig. 4). In 2016, samples were collected at 21 locations to cover accessible hillslope areas from the lowlands in a circular pattern. In 2017, only a limited number of samples were collected at six locations. The sampling was partly for confirmatory purposes at locations that had Cs-137 or soil-type anomalies in 2016. In 2018, the sampling campaign focused on the southwest slope, and the sample locations covered the entire slope. Additional samples on the eastern side were also collected in 2018. However, most of the sampling locations were

160 on the southwest slope because of the accessible walk routes from the hill bottom to the ridges. There were 46 total sampling locations. At eight locations, multiple-year samples were collected, and those measurements were averaged in this article. The total number of samples, including those multiple-year samples, was 58.

Figure 4. Sampling location developments through three summers (Basemap: Esri, DigitalGlobe. GeoEye, Earthstar Geographics, CNES/Airbus DS, USDA, USGS, AeroGrid, IGN, and the GIS user community).

The images in Fig. 5a–Fig. 5f show the study site's topography and sampling locations (yellow dots). The elevation change from the lowest to the highest sampling point was approximately 140 m (Fig. 5b). The 5 m interval contour lines in Fig. 5c were extracted from a 1 m digital evaluation model (DEM) using ArcMap 10.7.1 (ESRI Inc., 2019). The satellite imagery credit will be abbreviated as "ESRI" hereafter. The largest basin border at the study site (Fig. 5d) was extracted using the System for Automated Geoscientific Analyses (SAGA GIS; Conrad et al., 2015). The area of the largest basin is 0.56 km^2. The flow directions (Fig. 5e) were determined by the "D-infinity Flow Direction" tool of Terrain Analysis Using Digital Elevation Models (TauDEM; Tarboton, NA). As Fig. 5f – an image taken in winter – shows, the ground is exposed in winter except for areas with evergreen trees.

A soil sampler (diameter: 5 cm; length: 30 cm) from Daiki Rika Kogyo Co., Ltd., Japan, was used for soil sample collection. The tube was made of metal and contained a replaceable plastic liner. The sampler was pushed into the ground with a hammer. Once the sampler was fully inserted, it was pulled out and the plastic liner containing the soil was removed, sealed, and brought back to a laboratory at the University of Tokyo.
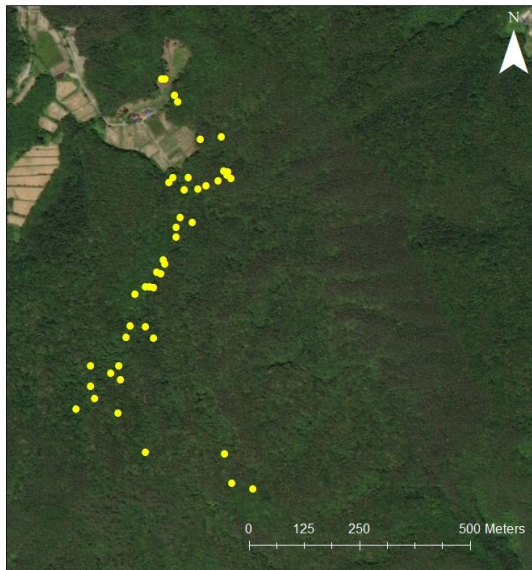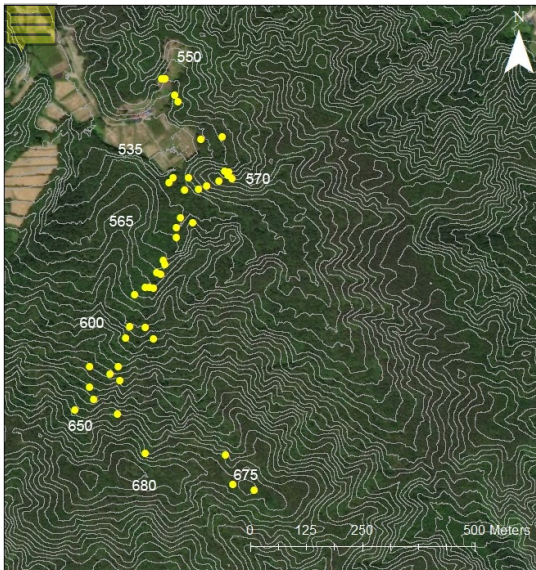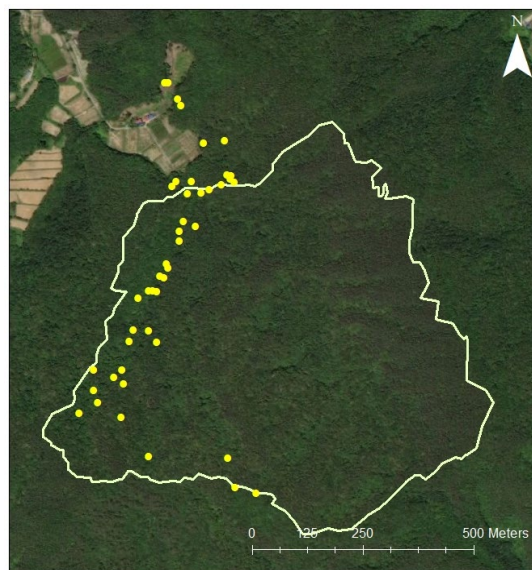
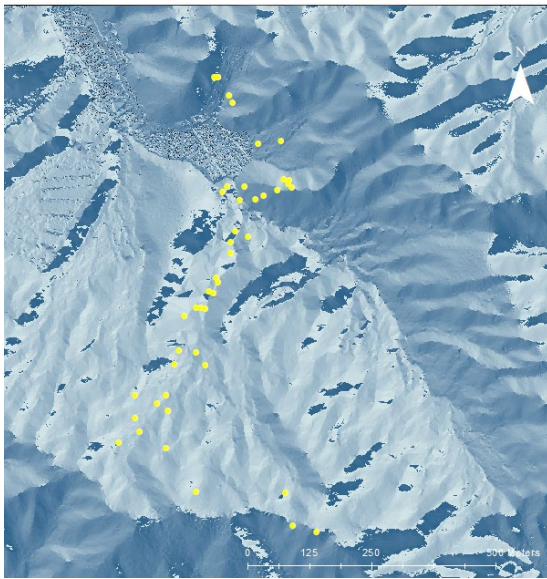**(5a) Aerial image of the study site (Basemap: ESRI).**
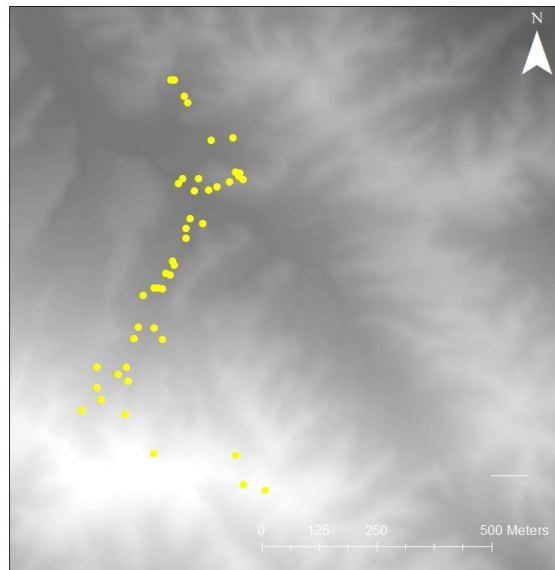
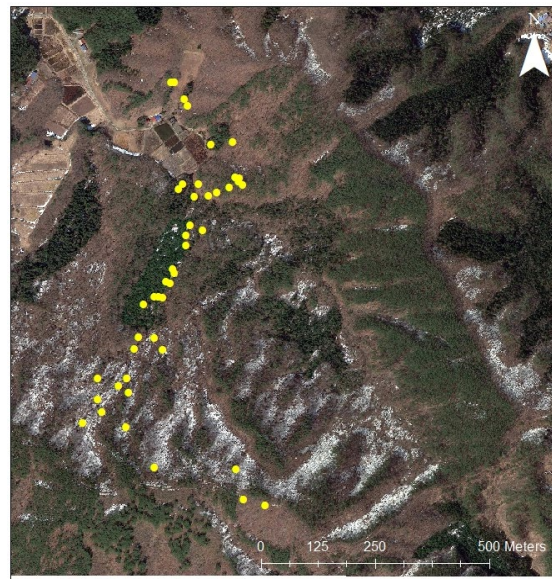**(5b) Elevation (m) profile of the study site.**

(5c) Contour lines of the study site (5 m interval) (Basemap: ESRI).

(5d) A large basin enclosing the longest slope (Basemap: ESRI).

11

(5e) Flow direction differences of the study site. (Darker colors flow between 135 and 315 degrees. Lighter colors flow between 315 and 135 degrees.)

(5f) Deciduous and evergreen vegetation at the study site as of 9 January 2017 (Map data: Google, Maxar Technologies).

Figure 5. Study site topography and aerial images.

3.2 Radioactivity Measurement

185　In the laboratory, each plastic tube was cut open with a knife, photographed, divided into 2.0 cm-thick disks (from the surface to 20.0 cm deep), and 2.5 cm thick disks (20.0–30.0 cm deep). In this article, the total value in an entire tube is called a "core total." When a sample contained visible pieces of plant roots or rocks, these pieces were removed. Each disk sample was placed on a plate, weighed, and dried in an oven for about 24 hours at 105°C. The drying time was extended if necessary to achieve consistent dryness across the samples. The dried sample was reweighed, placed in a mortar, and ground into fine

190　pieces. When the dried sample contained soil particles larger than 2.0 mm (that is, larger than the sand category), these particles were removed using a sieve. Other than these removals, no additional sorting or washing was applied.

Processed samples were stored in polyethylene vials and sent to the Isotope Facility for Agricultural Education and Research, Graduate School of the University of Tokyo, for isotope analysis. Radioactivity levels were measured with a NaI(Tl)

195　scintillation automatic gamma counter (2480 WIZARD2 gamma counter, PerkinElmer Inc., Waltham, MA, US), which was equipped with a well-type NaI(Tl) crystal (diameter: 3 in; length: 3 in) and covered with a 75 mm thick lead shield. Energy calibrations were performed using the 662 keV energy peak of gamma rays from Cs-137. It should be noted that "keV" is the abbreviation for "kiloelectron volts," a unit of energy in diagnostic radiography and nuclear medicine equivalent to the kinetic

energy gained by an electron falling through a potential of 1 volt. For radiocesium, the detection limit was approximately 0.5 Bq. After each measurement, the radiation was separated into radiation emitted by Cs-137 and Cs-134 using the abundance ratio of Cs-137 to Cs-134 at the time of sampling. That ratio was obtained from the physical decay rates of the isotopes and the elapsed time from the accident to sampling, assuming that the ratio at the time of the FDNPP accident was 1:1 (Nobori, et al., 2013, Tanoi, et al., 2019). Although a gamma-ray spectrometer provides more precise Cs-137 measurement data, lower-resolution NaI with effective algorithms can be quite effective and, thus, is preferred for its ruggedness, shorter time required for evaluation, and cost of operation (Burr and Hamada, 2009, Stinnett and Sullivan, 2013). The United States Environmental Protection Agency (US EPA) allows this NaI method for gamma-ray measurement during radioactive incident responses (EPA, 2012).

3.3 Soil property measurement

During soil processing in the laboratory, soil water content (%) and soil dry bulk density (g cm^{-3}) were calculated for each disk. Table 4 displays the depth layer averages of water content (%) and dry bulk density (g cm^{-3}), average standard deviations, and the average coefficient of variations (COVs: standard deviation/mean). In the top layer, the average water content percentage was above 100 % because some samples were collected in depressions and contained water exceeding field capacity. Dry bulk density was low (< 1.0 g cm^{-3}) throughout the depth, although it increased as the soil depth increased. This procedure could make the density smaller than the original sample. Organic matter removal occurred mostly in the surface soil, and rock removal occurred below the mid-depth. The number of the subjected samples was approximately less than 10 % of all samplesThe standard deviations of water content in the uppermost soil layers were large (> 50 %) and decreased in deeper soils– an opposite trend to the standard deviations of bulk density. The COVs of water content and bulk density were approximately the same in the top 4.0 cm. Both COVs decreased at the 6.0–10.0 cm depth then, once again increased toward the mid-depth of 16.0–20.0 cm. Figure 6 shows the measured value ranges, mean, median, and COVs of water content and dry soil bulk density. Water content percentages showed a wider variation (COV) than soil bulk density. The average bulk density of all the samples was 0.44 g cm^{-3}.
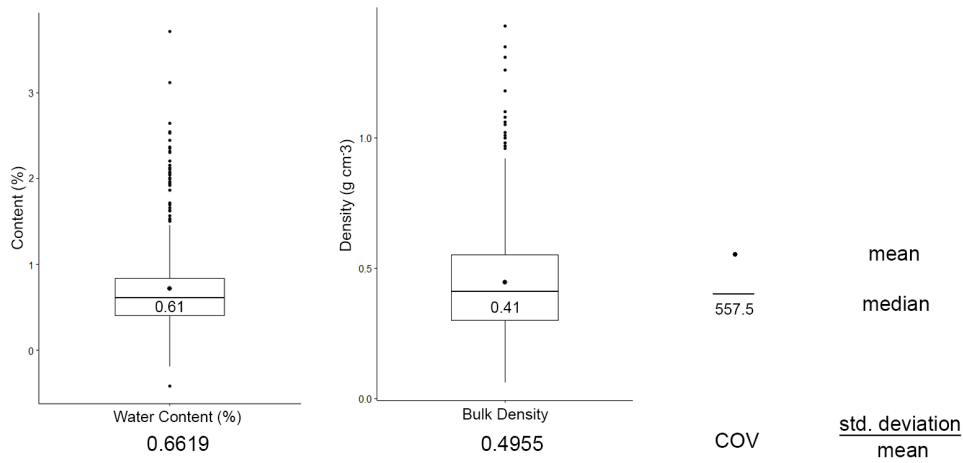
Previous studies have indicated that a soil's texture affects the amount of adsorbed Cs-137 per unit mass of soil particles and, thus, the accumulation patterns of Cs-137 in soils (Bennett et al., 2005; Giannakopoulou et al., 2007; Korobova et al., 1998; Walling and Quine, 1992). Thus, a portion of the soil samples was selected for soil texture testing (50 % of the sampling locations). Only some of the samples were tested for texture because of time and human resource constraints during the limited lengths of the first author's stays in Japan. The samples chosen for texture testing were selected so that they covered various soil types and colors and so that their locations were not concentrated at a certain elevation.

230

13

**Table 4. Soil properties of the samples by depths.**

Depth (cm)	Average water content (%)	Average bulk density (g cm^{-3})	Average standard deviation		Average COV	
			Water content (%)	Bulk density (g cm^{-3})	Water content (%)	Bulk density (g cm^{-3})
0.0–2.0	22	24	72	14	59	59
2.0–4.0	99	28	56	15	57	54
4.0–6.0	90	32	52	13	58	40
6.0–8.0	79	38	42	15	53	40
8.0–10.0	69	45	31	17	45	39
10.0–12.0	72	47	45	20	62	42
12.0–14.0	63	48	34	19	54	39
14.0–16.0	66	50	41	20	62	41
16.0–18.0	59	52	39	23	65	44
18.0–20.0	56	57	36	27	65	48
20.0–22.5	56	54	34	23	61	43
22.5–25.0	53	54	33	23	63	43
25.0–27.5	53	51	33	22	63	43
27.5–30.0	48	51	27	21	55	42

Figure 6. Measurement distributions of water content (%) and dry bulk density (g cm^{-3}).

235

On average, the tested soils contained more than 50 % sand, and most of the samples could be categorized as sand, loamy sand, sandy loam, and loam (Fig. 7).

14
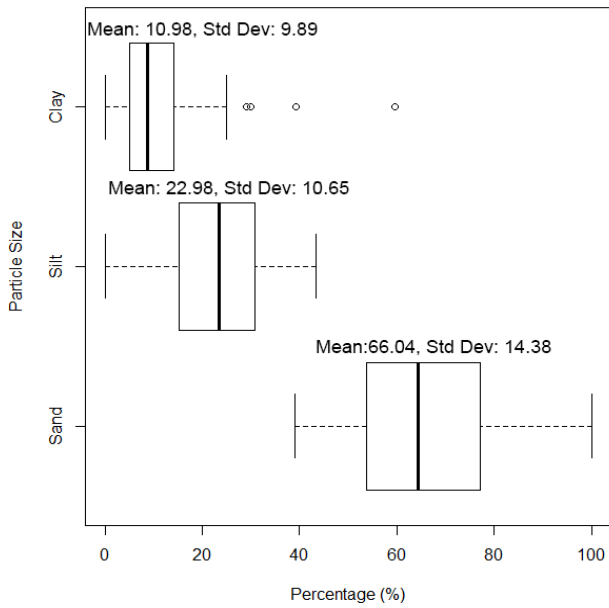
Figure 7. Percentages of clay, silt, and sand particles in the selected soil samples.

240

The average dry bulk density of all the samples was 0.44 g cm^{-3}, which is low for sandy soils. Figure 8 shows a core and disks of one of the collected samples. The average dry soil bulk density of the entire core was 0.94 g cm^{-3}. Soils in the site were brittle in general and granular.

245

Figure 8. A core and disks of one of the collected soil samples.

4 Data

4.1 DEMs

250 In this study, the topographic effects were examined via two DEMs with different spatial resolutions: 1 m and 10 m. Certain topographic features depend on spatial resolutions, and using multiple DEMs enables researchers to identify resolution dependency (Gallant and Wilson, 1996, Kim and Lee, 2004, Moore, et al., 1993). The 1 m resolution DEM was provided by Forest Research and Management, Japan. Its original datum was GCS JGD 2011 (Zone 9), and the data collection year was 2012. The 10 m resolution DEM was downloaded from the website of the Geospatial Information Authority of Japan

255 (https://www.gsi.go.jp/kiban/). Its file date was 1 October 2016. The 10 m DEM was generated by the Japanese government, and the original datum was GCS JGD 2000. The coordinate projection of all GIS files, including DEMs, was set to UTM 54N in this article.

4.2 Topographic parameters

The following list shows the original parameters used in this analysis as well as the guiding assumption behind the parameter

260 selection.

16

1) **Elevation:** Soil particles, by which Cs-137 is adsorbed, move downward on a sloped surface. Thus, Cs-137 levels are higher in downslope areas (Martin, 2000, Roering, et al., 1999).

2) **Slope degrees, upslope distance to a basin edge:** Relating to elevation, at a certain point on a hillslope, Cs-137 levels are controlled by slope degrees and the length of the hillslope above that point (Komissarov and Ogura, 2017, Roering, et al., 2001, Roering, et al., 1999).

3) **Distance from the hill bottom:** Relating to elevation, hypothetically, the closer a sampling point is to the bottom of a hill, the higher the Cs-137 levels.

4) **Surface plan curvature, topographic wetness index (TWI):** Cs-137 migrates through the subsurface in soils by infiltration. Thus, where water pools, at the flat or concave surface, Cs-137 levels are higher and have migrated to a further depth (Schimmack, et al., 1994, Schimmack, et al., 1989, Teramage, et al., 2014). In general, slope degrees and curvatures – particularly profile and plan curvatures – are considered some of the most influential factors in hydrology and soil transport on a sloped surface; hence, they also influence Cs-137 movement (Gessler, et al., 1995, Heimsath, et al., 1997, Momm, et al., 2012, Moore, et al., 1993, Tesfa, et al., 2009). Topographic wetness is one of the two most powerful and most frequently used surface hydrology indices, along with the stream power index (Hengl and Reuter, 2008).

5) **Vegetation cover, hillslope aspect (categorical parameters):** If topographic factors and soil properties do not explain Cs-137 concentrations, other factors could be involved, such as vegetation cover (Coughtrey, et al., 1989, Hashimoto, et al., 2013, , Wakai, et al., 2019) and locational differences (e.g., opposite sides of the main channel with opposite aspects) (Gellis and Walling, 2011, Istanbulluoglu, et al., 2008, Korobova and Romanov, 2009, Wicherek and Bernard, 1995).

In the current study, Cs-137 values were reported in two units: Bq kg^{-1} (absolute measurement) and Bq m^{-2} or mass depth (Bq kg^{-1} × dry bulk density × sample thickness). Since soil bulk density varies across samples, mass depth indicates the functionality of soil bulk density as an explanatory variable, and it also provides a means to compare concentration levels among samples with varied soil bulk densities (Kato, et al., 2012, Miyahara, 1991, Rosén, et al., 1999).

A preliminary check of autocorrelation among topographic parameters revealed that elevation and distance from the hillslope bottom were highly correlated because of the vertical spatial configurations of sample locations. Thus, distance from the hillslope bottom was removed from parameter selection and, in total, five topographic parameters, two soil properties, and two categorical parameters were used in the subsequent analysis (Table 5).

Table 5. List of data and parameters used in this study.

Data and parameters categories	Description
Cs-137	Bq kg^{-1}, Bq m^{-2}

17

Topographic parameters	elevation (m), slope degrees, upslope distance (m), plan curvature, TWI
Soil properties	water content (%), bulk density (g cm^{-3})
Categorical	vegetation cover types, aspect

4.3 Parameter Extractions

4.3.1 Elevation

The elevation of sampling locations was extracted from the DEMs using the raster::extract function of R (R Core Team, 2015).

4.3.2 Slope Degrees, Plan Curvature, Upslope Distance

SAGA GIS (Conrad et al., 2015) was used to compute slope degrees and plan curvature. SAGA was chosen because of its multiple options for the curvature calculation setting. The method used for plan curvature calculation was the second-order polynomial based on elevation values in nine surrounding cells (Zevenbergen and Thorne, 1987). The "D-Infinity Distance Up" tool of TauDEM (Tarboton, NA) was used to compute the upslope distance (Tarboton, 1997). This tool calculates the distance from each grid cell up to the ridge cells according to the reverse D-infinity flow directions. Multiple options for upslope calculations are provided in the tool. In this study, both "minimum" distance and "surface" distance calculation options were used.

4.3.3 TWI

TauDEM was used to calculate TWI values. The TWI tool calculates the ratio of the natural log of the specific catchment area (contributing area) to the slope. The index reflects water's tendency to accumulate at any point in the catchment and gravitational forces' tendency to move the water downslope (Quinn, et al., 1991). No data values occur in locations where the slope is 0. TWI was calculated as follows (Quinn, et al., 1991, Quinn, et al., 1995) (Eq. 1):

$$TWI = \ln\left[\frac{A}{\tan(\beta)}\right] \tag{1},$$

where TWI is the topographic wetness index, A is the total upslope area accumulated in the current cell, and β is the hillslope gradient. All topographic calculations in SAGA and TauDEM were saved as .TIF files. Then, the "raster::extract" function of R was again used to extract each topographic value for sampling locations.

4.3.4 Vegetation cover type

For vegetation data, color winter imagery was downloaded from Google Earth (source image provided by Maxar Technologies). The date of the imagery was 9 January 2017. Vegetation categories (evergreen or deciduous) were classified using the ArcGIS 10.7.1 image classification tool (ESRI Inc., 2019).

4.3.5 Sample grouping by hillslope aspects

Based on the flow direction map (Fig. 5e), soil samples were divided into two groups: samples on the east side hillslopes (southwest facing) and samples on the west side hillslopes (northeast facing) of the main channel. Although the aspect at each sample location (raster cell) might differ even on the same side, authors use a simple categorization due to the small number of samples.

5 Methods

The selection of sampling locations in this study was influenced by the terrain or accessibility, and this selection was not random or uniform. Thus, using distance-based spatial analysis – such as a semivariogram – was determined not to be appropriate, and a numerical regression approach was adopted.

5.1 Statistical analysis for the effects of topographic parameters

5.1.1 Generalized additive models (GAM)

As a preliminary step, regression methods (linear, polynomial, logarithm, and bi-splines) were tested on Cs-137 measurements in both Bq kg^{-1} and Bq m^{-2} units, using the five topographic parameters. The results showed that the polynomial and bi-splines methods returned higher R^2 values than the other methods. Resulting plots showed that the fitting curves had multiple knots that generated waveforms. Meanwhile, descriptive statistics indicated the exponential distribution and outliers of Cs-137 values (see Sect. 6.1). All parameters had different ranges of numbers and precisions. Thus, a more flexible regression method was sought, and the authors decided to use the generalized additive models (GAM) (Clark, 2013, Tesfa, et al., 2009, Wood, 2017). GAM is a generalized multiple linear regression involving a sum of smooth functions of covariates or fitting functions. Eq. 2 below explains the basic concept of the GAM model (Wood, 2012).

$$g(\mu_i) = A_i\theta + f_1(x_{1i}) + f_2(x_{2i}) + f_3(x_{3i}) + \cdots f_k(x_{ki}) \tag{2},$$

where $x_1, x_2, \ldots, x_k$ are explanatory variables (predictors); $\mu_i \equiv \mathbb{E}(expected)(Y_i)$ and $Y_i \sim EF(\mu_i, \phi)$, Y_i are response variables; $EF(\mu_i, \phi)$ denotes an exponential family distribution with mean μ_i and a scale parameter, ϕ; A_i is a row of the model matrix (parametric); and θ is a corresponding parameter vector. Finally, f_j are smooth functions (non-parametric) of the covariates of x_k.

For actual calculations and data output, the R packages mgcv and gamair (Wood, 2012) were used. GAM attempts to simultaneously minimize overfitting and underfitting by calculating multiple coefficients in a model. Users can select a smoothing function (basis) for the entire model or for each variable. They can also select fitting methods ("method") and the

number of knots ("k"), a distribution model type ("family"), and a relationship between means of variables ("link"). Adding a categorical term ("identity") to the model is possible. GAM outputs parametric coefficients, R^2, p-values, a deviance-explained percentage, and generalized cross-validations (GCVs) (Eq. A1) for the model, as well as the approximate significance of smooth terms for each variable.

Although GAM has a weakness in that users cannot retrieve an individual regression expression from the output, it has been used in soil and Cs-137 research (Linnik, et al., 2020, Tesfa, et al., 2009). This study used a spline-based smooth term for each parameter (variable). The GAM setting was consistent for all model runs (see Appendix A-B).

Following the single-parameter GAM analysis, combinations of parameters were tested with GAM to determine the degree to which these parameters explain Cs-137 concentrations. Combinations with more than three parameters were not tested to avoid overfitting and to identify parameters that have a distinct influence on Cs-137 levels. The total number of combinations was 63 – the permutation of seven parameters with five topographic parameters and two soil properties, not considering the parameter orders. Thus, the models included those with only topographic parameters, those with only soil properties, and those in which both parameters were mixed.

To reflect the vertical profile of Cs-137 concentrations, GAM models were run against each depth layer. Thus, for topographic parameters with one distinct value for the entire core sample, such as elevation and slope degrees, the runs employed a "one to many" relationship (topographic parameters to Cs-137 in multiple depth layers). For soil properties with a measurement for each depth layer, the runs employed a "one to one" relationship (soil property in a depth layer to Cs-137 in the depth layer).

5.1.2 GAM checks

The accuracies of these predictions were checked via the statistical indices that GAM returns with a "gam.check ()" function. Outlier samples, which influenced predictions, were checked with Cook's distance (Cook, 1977) (Eq. 3). (Stevens, 1984) stated, "Cook's distance measures the joint (combined) influence on the case being an outlier on y and in the space of the predictors."

$$D_i = \frac{\left(\hat{\beta}_{(-i)} - \hat{\beta}\right)' \mathrm{X}'\mathrm{X}\left(\hat{\beta}_{(-i)} - \hat{\beta}\right)}{ps^2} \quad i = 1, 2, \dots n \text{ (Cook, 1977)} \tag{3},$$

where D_i is Cook's distance, $\hat{\beta}$ is the estimated regression coefficient, $'$X is the transpose matrix of n × p known constants, ρ is the number of predictors, and s^2 is the variance.

5.2 The effects of vegetation cover and hillslope aspects

To determine the effects of vegetation and locational differences on Cs-137 level predictions, an interaction term ("by=") was added to the GAM models since vegetation and locational differences are categorical data (e.g., evergreen or deciduous areas). Then, the significance of the models was compared pair-wise with a Tukey's honestly significant difference (HSD) post hoc test (Tukey, 1949). This test runs an analysis of variance (ANOVA) and then compares the means of parameter pairs (Eq. 4).

$$q = \frac{m_1 - m_2}{sm} \text{ (Tukey, 1949)} \tag{4},$$

where q is the Tukey HSD result, m_1 is the larger of the means compared, m_2 is the smaller of the means compared, and sm is the standard deviation of the means. R's "TukeyHSD ()" function returns the differences in means, confidence levels, and adjusted p-values for each pair. The confidence interval in this study was 0.95. When the resulting interval overlaps the zero point of the confidence interval, the difference between the pair is not significant.

5.3 Spatial extrapolation

Since practical decontamination planning requires a contamination estimate for an entire target area, it is important to determine whether the best performance model works for the spatial estimation of Cs-137 levels. As the last step, a selected GAM model was extrapolated to a basin in the study area, and the results were compared with the initial fallout deposition estimated by the Japanese government and the United States Department of Defense (MEXT, 2011). For this step, GAM's "predict()" function loaded topographic parameters in stacked raster files and predicted Cs-137 values in each raster cell based on the selected model. The "predict ()" function was repeated for each depth layer. Then, the total Cs-137 concentration, down to 30 cm deep, was calculated by summing the Cs-137 values in all layers.

6 Results

6.1 Cs-137 concentration levels

This section overviews the Cs-137 levels in the soil samples. Going forward, Cs-137 values in this article are decay-normalized to 28 June 2016 (Eq. A1 and Eq. A2).

Figure 9 shows the distributions of core total Cs-137 values in kBq kg^{-1} (red) and kBq m^{-2} (gray), as well as their means. The y-axis is the number of core samples in each Cs-137 value bin (200 k). When Cs-137 was measured in kBq kg^{-1}, the Cs-137 values concentrated in six bins, and 44 % of the core samples were in the 200–400 kBq kg^{-1} bins. In the mass depth unit (kBq m^{-2}; gray), the distribution curve became flatter. In both cases, the above-average values had longer tails. The average total

core Cs-137 values among these samples were 271 kBq kg⁻¹ and 1,087 kBq m⁻². The same data on a log scale (Fig. 10) shows

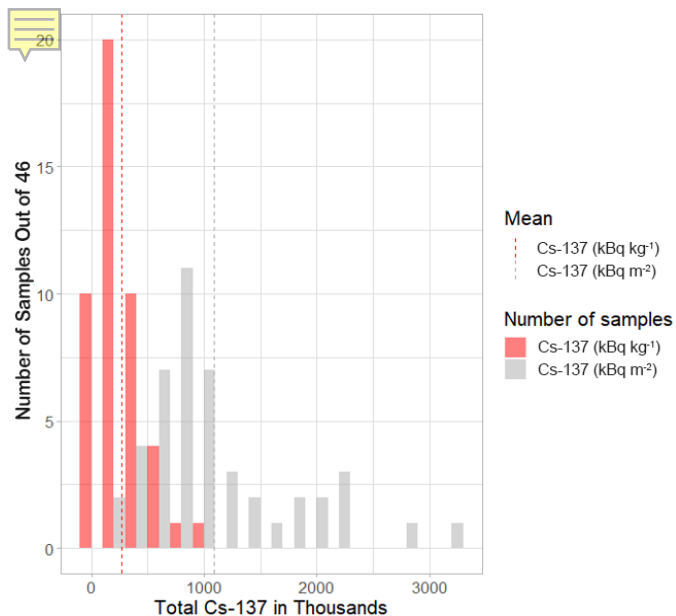400   that the distributions become close to a normal distribution; however, the curves are not smooth.

Figure 9. Distribution of total Cs-137 in a core sample (red: Cs-137 kBq kg⁻¹; gray: Cs-137 kBq m⁻²). A unit of each bin is 200 k.
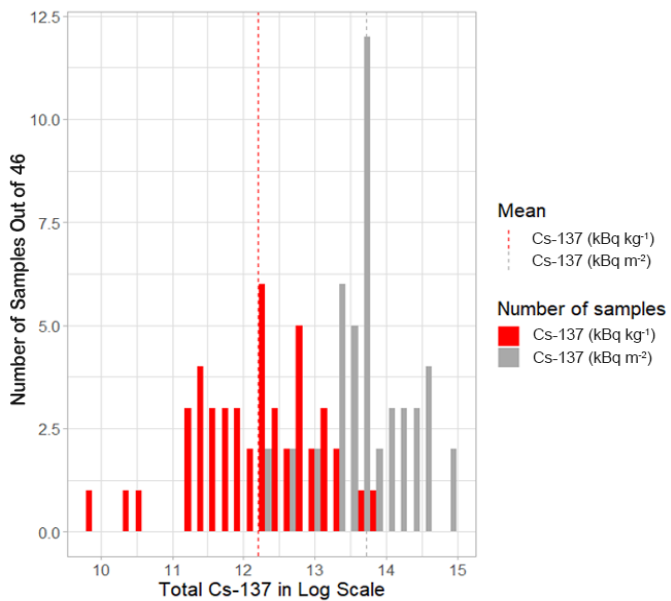

Figure 10. Distribution of total Cs-137 in a core sample in a log scale (red: Cs-137 kBq kg⁻¹; gray: Cs-137 kBq m⁻²).

405

Depth distributions of Cs-137 in both kBq kg^{-1} and kBq m^{-2} (Fig. 11) show exponential vertical decreases, similar to the results reported in previous Cs-137 research (Fujii, et al., 2014, Koarashi, et al., 2012, Matsunaga, et al., 2013, Takahashi, et al., 2015, Tanaka, et al., 2012, Teramage, et al., 2014). These samples were collected five to seven years after the FDNPP accident, and they still held large portions of Cs-137 in the top layers. The average depth of 90 % concentration (90 % of the whole Cs-137 in a core sample) was 7.45 cm. Standard deviations in the upper layers were large, up to 115 kBq kg^{-1} and 335 kBq m^{-2} in the top 2 cm (red dots in Fig. 12 and Fig. 13). However, the COVs were below 100 % in the top layer (gray dots in Fig. 12 and Fig. 13). The COVs increased toward the 14–16 cm depths (Fig. 12 and Fig. 13). One reason for the COV increase in the deepest two layers could be the variability in Cs-137 migration head depths among samples (Fig. 16).
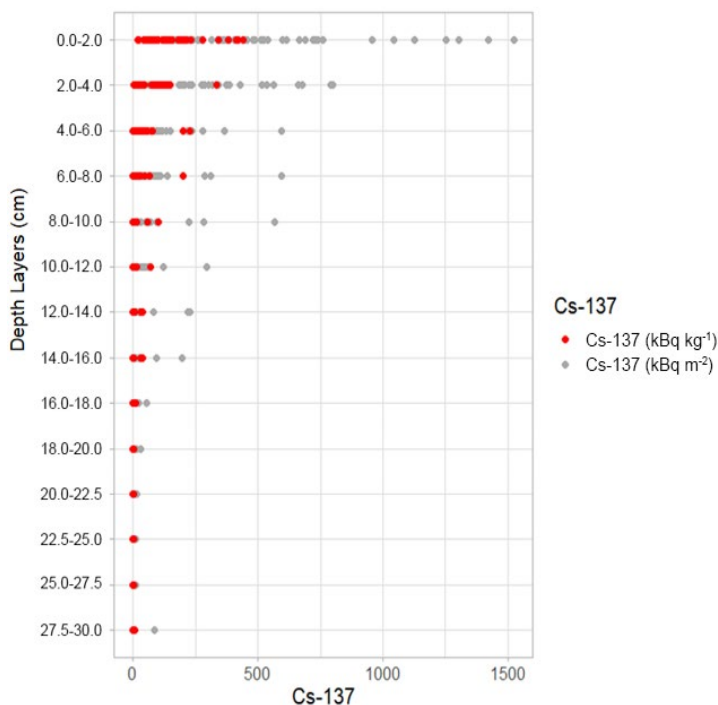
Figure 8. Depth distribution of Cs-137 in kBq kg^{-1} (red) and kBq m^{-2} (gray).
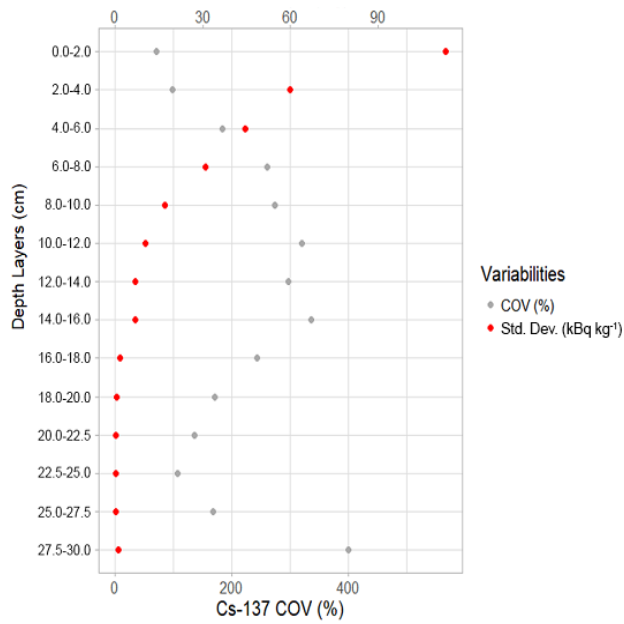
23

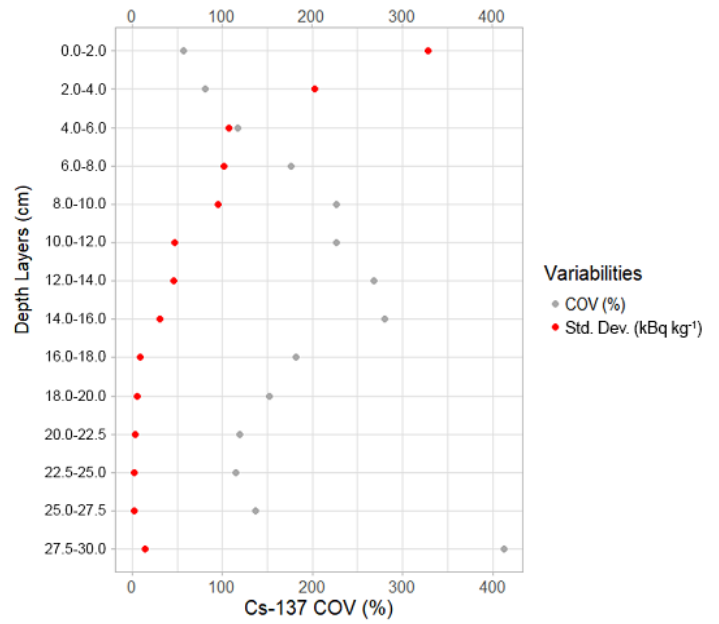**Figure 12. Standard deviations (red) and COVs (gray) by depths in kBq kg^{-1}.**

Figure 13. Standard deviations (red) and COVs (gray) by depths in kBq m^{-2}.

6.2 Test 1 results: Cs-137 accumulation patterns on a simple representative hillslope

This section displays the Cs-137 accumulation levels on a simple representative hillslope. The following three graphs (Fig. 13–Fig. 15) organize the total core Cs-137 concentrations of all samples by one topographic parameter (elevation in meters). In Fig. 13–Fig. 15, red circles are added to indicate the four highest concentration samples in Bq m^{-2} and to compare their Cs-137 values and elevations (Fig. 13), slope degrees (Fig. 14), and migration head depths (Fig. 15).
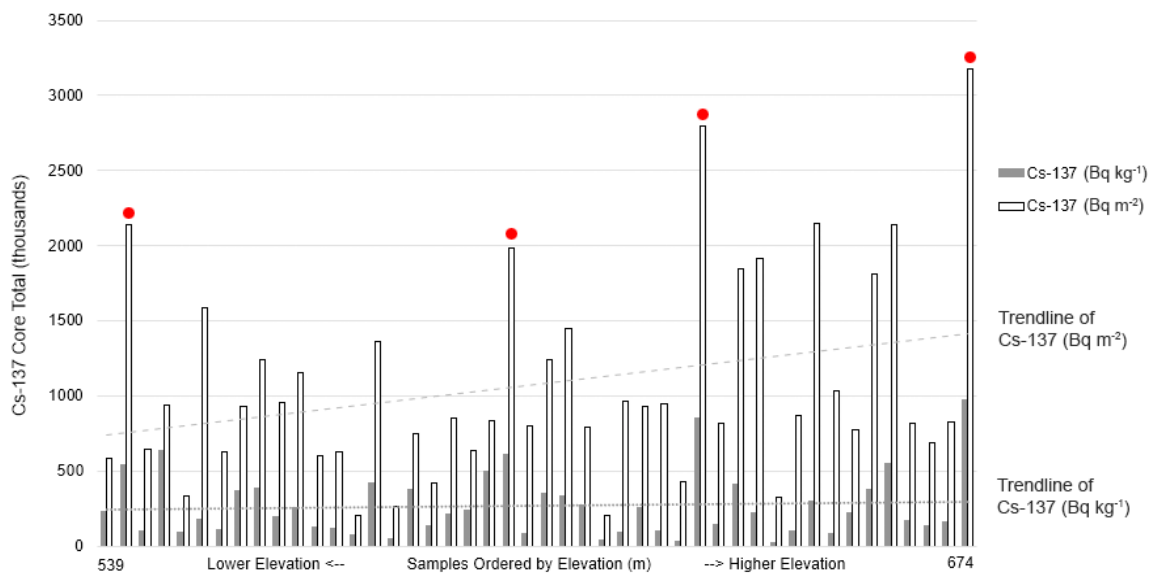
420

24

Figure 14. Core total Cs-137 concentrations in both units along elevation (m).
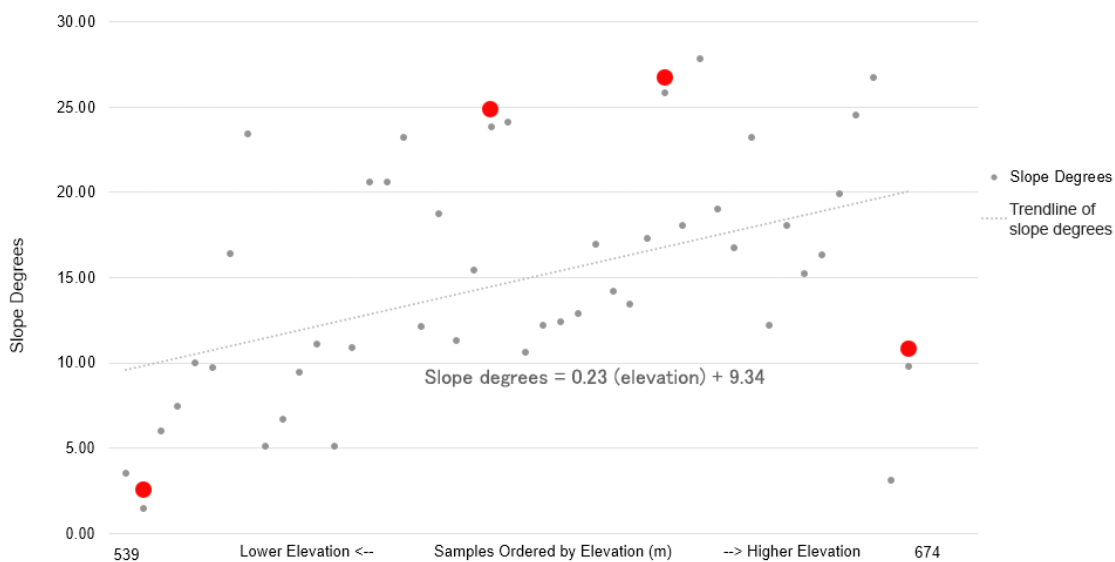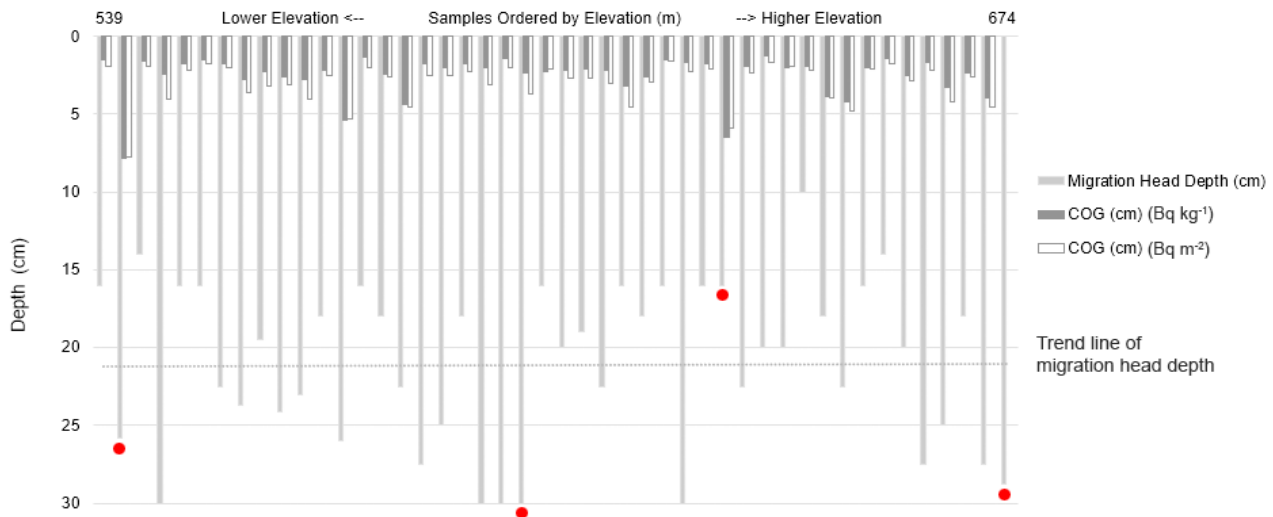
425

Slope degrees = 0.23 (elevation) + 9.34

Figure 15. Slope degrees of sampling points along elevation (m).

25

Figure 16. Migration head depths (cm; the depth at which Cs-137 decreased to 100 Bq kg⁻¹ in each core sample) and the depths of COGs (cm) in each core sample for both units (Bq kg⁻¹ and Bq m⁻²).

In Fig. 13, both trend lines of Cs-137 in Bq m⁻² values show upward trend along elevation. However, the actual Cs-137 level presents a "camelback" shape. Figure 14 shows slope degrees at each sampling location along elevation. The trend line indicates an increase in slope degrees along elevation. However, the Pearson's correlation index between elevation and slope degrees was 0.24 due to the outliers at the ridge top and at the hill bottom.

Figure 15 graphs the migration head depth (cm) and the center of gravity (COG) depth (cm) for each core sample. The conservative background contamination level of the study site was 100 Bq kg⁻¹. Thus, the depth at which Cs-137 decreased to 100 Bq kg⁻¹ was considered the deepest level to which the FDNPP accident–derived Cs-137 had migrated downward. In four samples, the migration head had already reached 30 cm deep (the length of the sampling tube) in 2016. The average depth of the migration head was 20cm.

In Fig. 15, the COG depth was added to show relative downward migration rates. COG depth is not the depth of the largest Cs-137 concentration in the core sample; rather, it is the depth of the center of the Cs-137 concentration density. It is calculated as below (Shiozawa, et al., 2011) (Eq. 4).

$$(x) = \frac{\sum_i x_i C_i \Delta x_i}{\sum_i C_i \Delta x_i} \tag{4},$$

where x_i is the middle depth of each depth layer, C_i is the Cs-137 concentration of each depth layer, and Δx_i is the depth of each layer. The average COG depths in Bq kg⁻¹ and Bq m⁻² were 2.53 cm and 3.02 cm, respectively. As with the core total of Cs-137 in Fig. 13, the actual measurement showed a camelback shape along elevation. According to a Pearson's correlation

26

index, core total Cs-137 concentration levels in Bq kg^{-1} and the migration head depths were correlated (0.68), and Cs-137 in Bq m^{-2} and migration head depths were weakly correlated (0.45). The COG depths did not show significant correlations with the core total of Cs-137, indicating a discrepancy between the deepest reach of contamination and the relative depth of the highest concentration after several years since the initial fallout.

6.3 Test 2 Results: The effects of topographic parameters on Cs-137 accumulation patterns

6.3.1 Parameter ranges by DEM resolutions

This section displays the differences between topographic parameter values extracted from the 1 m and 10 m DEMs. Figure 17 shows the value ranges of each topographic parameter by DEM resolution. The numbers on the top row under each graph indicate COVs. The numbers on the bottom rows are the differences of medians between two DEMs divided by the range of all values of the parameter. As evidenced in the graphs, DEM resolution differences caused considerable data-range variations in the upslope distance and TWI. Plan curvature displayed a smaller disparity between the DEMs, but the range of values was approximately four times larger with the 1 m DEM compared to the 10 m DEM, while the COV was 6.5 times larger with the 10 m DEM.
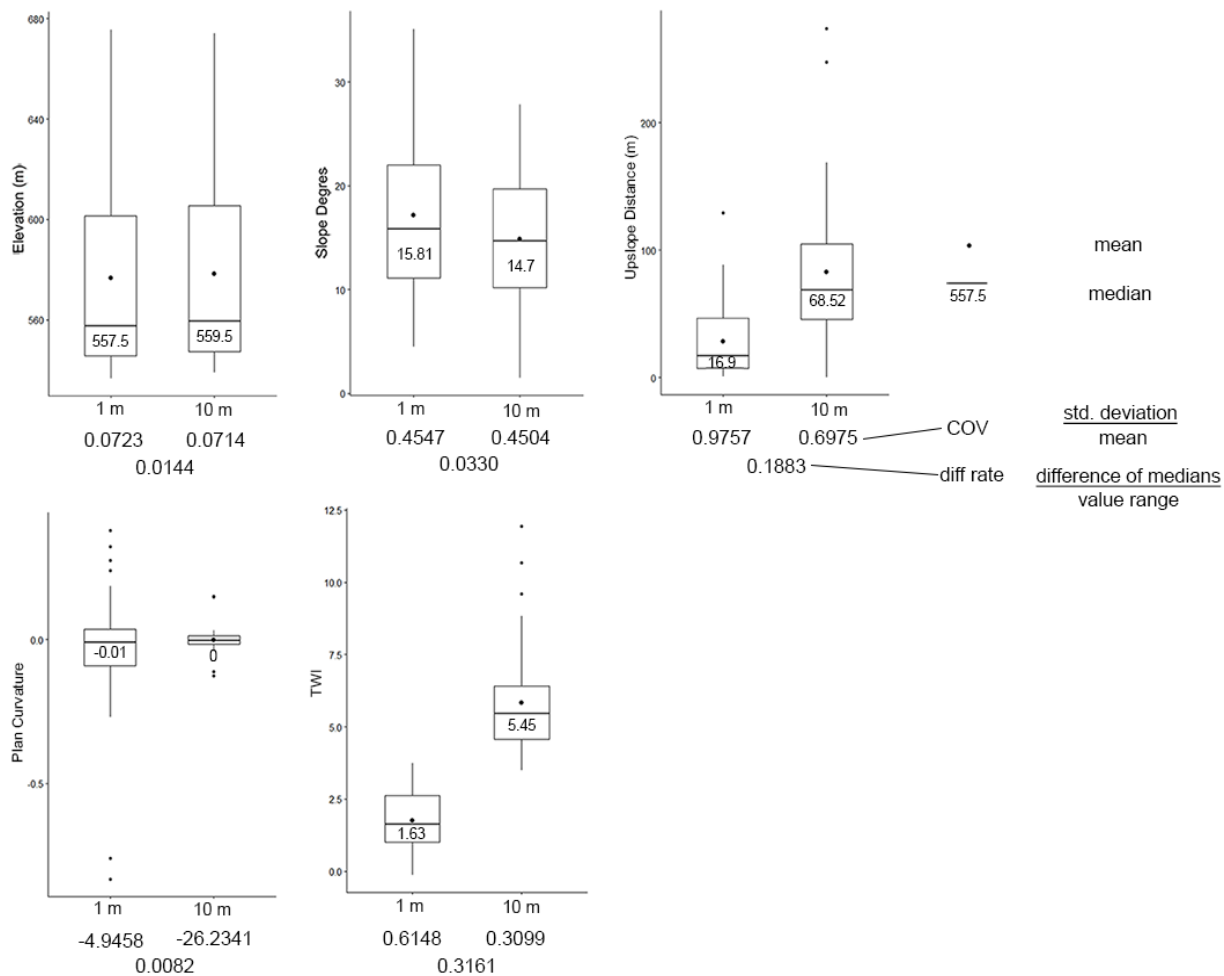
Figure 17. Topographic parameter distributions. Two box plots are presented for parameters affected by different DEM resolutions.

6.3.2 GAM results: Single parameter

465 This section reports the GAM results of the single-parameter models to determine each parameter's explanatory power for Cs-137 concentrations. In all instances of GAM, each model was run against each depth layer, and the averages of deviance explained percentages throughout the depths were calculated (Table 7). For p-values, since there is a clear cut point for significance ($p \leq 0.05$), the number of depth layers, whose p-values were equal or less than 0.05, are reported (e.g., "4/14" means that four depth layers' p-values were ≤ 0.05.). Table 6 includes the results of topographic parameters, which were

470 affected by the DEM resolutions, while Table 7 displays the results of soil property parameters, which were unaffected by the DEM resolutions. None of the single parameters in either table returned deviance-explained percentages above 36 % (which was found via a model including water content). The lowest p-value was 0.05, which was significant and also found via a

model with water content. Among the topographic parameters, TWI was the most effective with the 1 m DEM, while slope degrees were the most effective with the 10 m DEM. Soil properties, especially water content, demonstrated higher explanatory power than topographic parameters. However, although the p-values of soil properties were significant in more than ten depth layers in Bq kg^{-1} units, their significance decreased in Bq m^{-2} units. All parameters showed slightly higher explanatory power in Bq kg^{-1} than in Bq m^{-2}, except for plan curvature extracted from the 10 m DEM.

Table 6. The results of single topographic parameter GAM models for deviance-explained percentages and the number of depth layers where p-values were at 0.05 or below. "( )" indicates standard deviation.

1 m DEM				
Parameter	Deviance explained (%)	# of layers: p-value ≤ 0.05	Deviance explained (%)	# of layers: p-value ≤ 0.05
	Bq kg^{-1}		Bq m^{-2}	
elevation (m)	20.63 (14.49)	1/14	19.59 (13.06)	2/14
upslope dist. (m)	13.32 (14.41)	0/14	8.65 (13.24)	0/14
slope degrees	18.78 (22.76)	1/14	8.94 (18.34)	1/14
plan curvature	17.22 (14.63)	2/14	16.23 (11.85)	0/14
TWI	27.35 (20.78)	2/14	22.70 (1804)	3/14
10 m DEM				
Parameter	Deviance explained (%)	# of layers: p-value ≤ 0.05	Deviance explained (%)	# of layers: p-value ≤ 0.05
	Bq kg^{-1}	Bq m^{-2}	Bq kg^{-1}	Bq m^{-2}
elevation (m)	22.18 (13.28)	0/14	19.24 (11.55)	014
upslope dist. (m)	22.69 (17.26)	3/14	18.16 (17.64)	2/14
slope degrees	28.31 (18.36)	7/14	22.38 (1755)	6/14
plan curvature	3.83 (5.26)	0/14	4.95 (7.98)	0/14
TWI	27.64 (17.92)	1/14	22.80 (2083)	1/14

29

Table 7. The results of single-soil-property-parameter GAM models for deviance-explained and the number of depth layers where p-values were at 0.05 or below. "( )" indicates standard deviation.

Parameter	Deviance explained (%)	# of layers: p-value ≤ 0.05	Deviance explained (%)	# of layers: p-value ≤ 0.05
	Bq kg^{-1}		Bq m^{-2}	
water content (%)	36.16 (20.21)	12/14	27.75 (24.60)	8/14
bulk density (g cm^{-3})	31.79 (17.02)	10/14	17.93 (16.83)	5/14

485

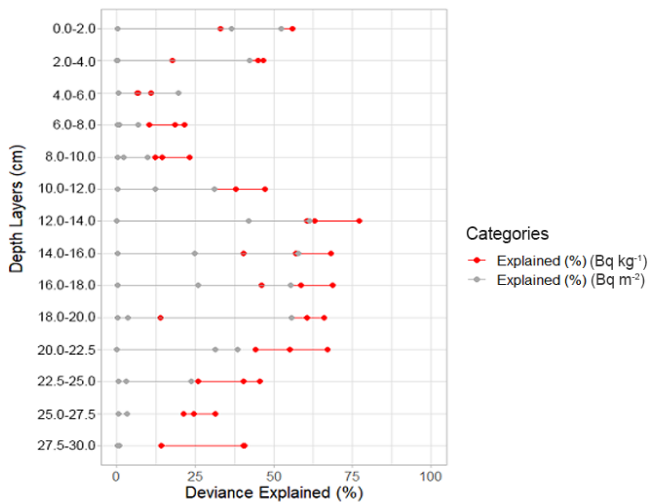### 6.3.3 GAM combination parameters results

Figures 18–23 show the percentages of deviance explained by depth layers, including one, two, and three-parameter models. In these figures, deviance-explained percentages were used instead of p-values because the authors wanted to determine the extent to which the variability of Cs-137 values was explained, rather than to test a simple model significance. The deviance-

490 explained percentages and p-values were in accordance; that is, higher explanation percentages returned lower p-values. In all six figures, the red dots represent the explanation percentages of Cs-137 in Bq kg^{-1} units and the gray dots represent the percentages of Cs-137 in Bq m^{-2} units.
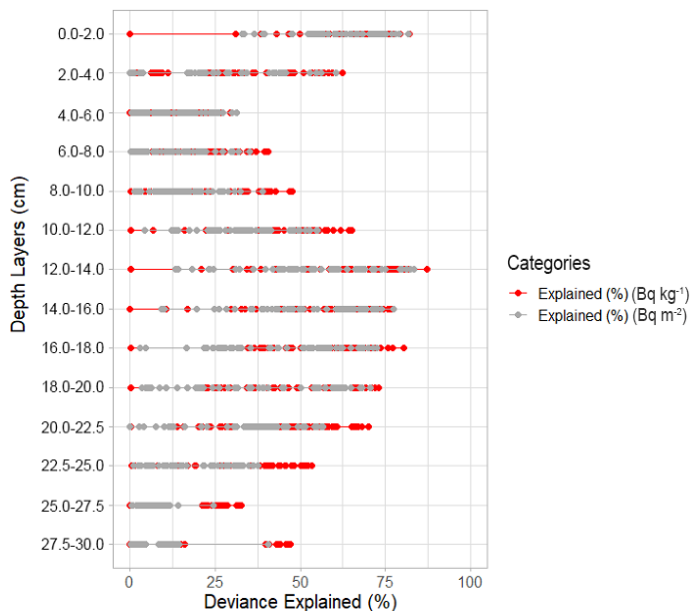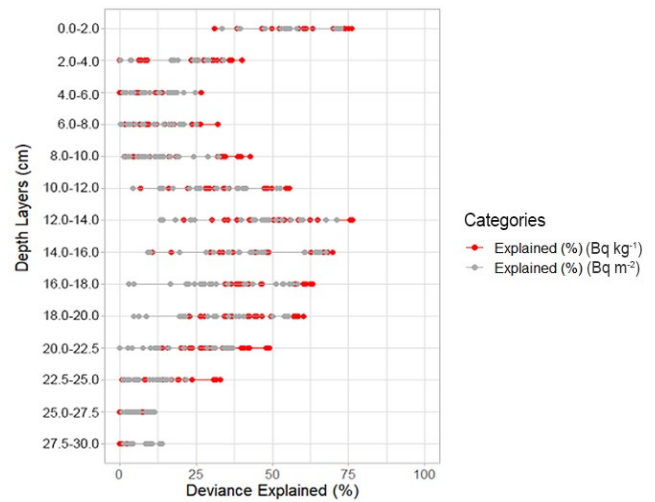

495 **Figure 9. Deviance explained (%) using the 1 m DEM.**

Figure 10. Deviance explained (%) using the 1 m DEM with soil properties only.

Figure 20. Deviance explained (%) using the 1 m DEM with topographic parameters only.

Figure 18 includes the results of using the 1 m DEM for all 63 combinations. The next two figures present the deviance-explained percentages using the 1 m DEM with only water content and bulk density (Fig. 19) and with only topographic parameters (Fig. 20). Figure 21 includes the results of using the 10 m DEM with all 63 combinations. The next two figures show the percentages using the 10 m DEM with only water content and bulk density (Fig. 22) and with only topographic parameters (Fig. 23).

Overall, the models using Bq kg^{-1} (red dots) returned better predictions than those using Bq m^{-2} (gray dots), and the models with the topographic parameters extracted from the 10 m DEM performed better than those using the 1 m DEM. However, in the topographic models based on the 10 m DEM, the low-end outliers became distinct (see gray dots in Fig. 21–Fig. 23).

All six figures showed similar vertical S-curves. The deviance-explained percentages of some models were over 75 % for the top layer (0.0–2.0 cm). The percentages declined below the top layer and rose again around a depth of 10.0–20.00 cm. This S-shape resembles the vertical profiles of the COVs for water content and bulk density (Table 4) and the COVs of the Cs-137 measurements (Fig. 12–Fig. 13). Models with only soil properties and models with only topographic parameters returned similar vertical curves (Fig. 19–Fig. 20; Fig. 22–Fig. 23).
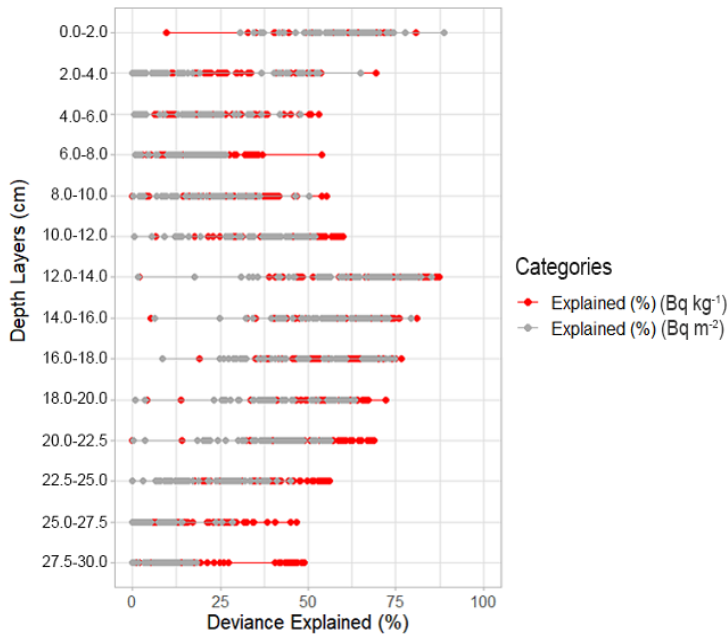
510

Figure 21. Deviance explained (%) using the 10 m DEM.
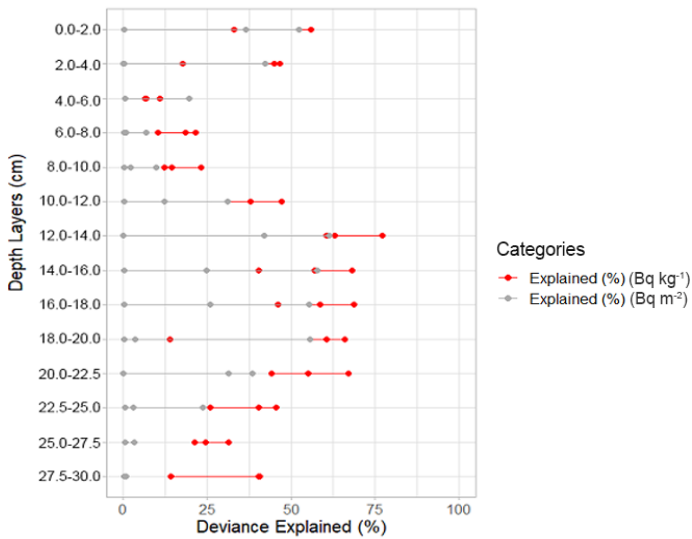

Figure 22. Deviance explained (%) using the 10 m DEM with soil properties only (same graphics as Figure 19. Repeated for comparison purpose).
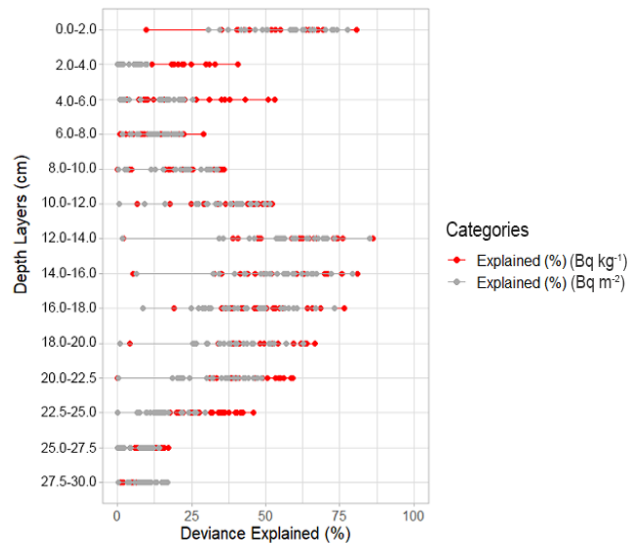

Figure 23. Deviance explained (%) using the 10 m DEM with topographic parameters only.

32

Table 8. The most effective parameter combinations with the best deviance-explained percentages and the number of depth layers where p-values were at 0.05 or below. "( )" indicates standard deviation.

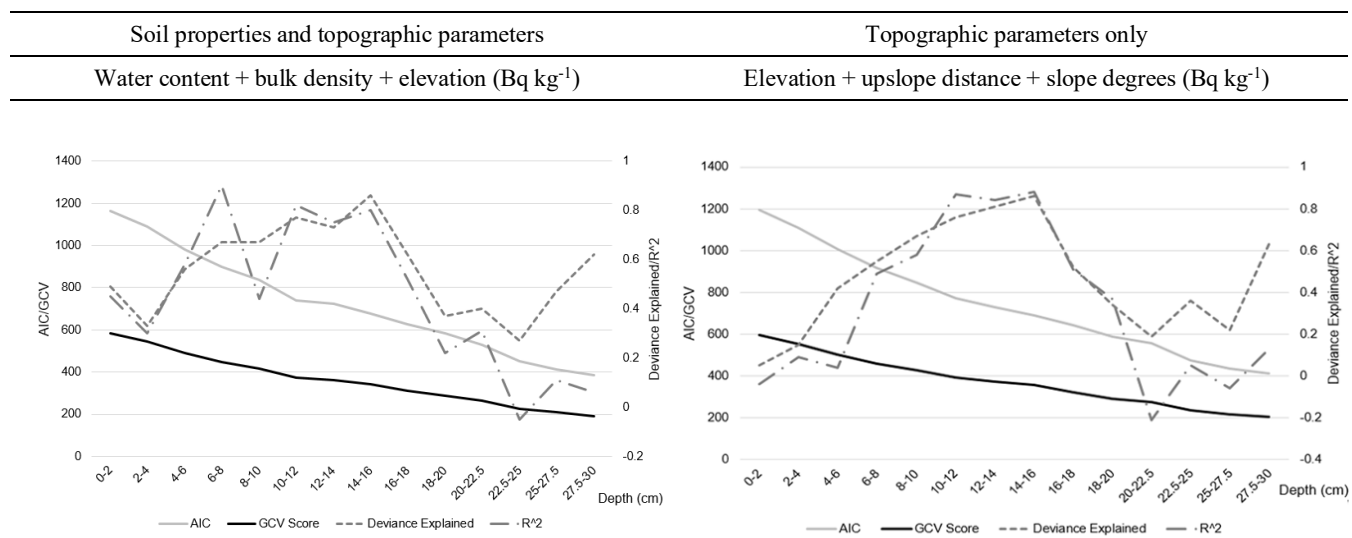| 1 m DEM							
	Parameter combinations	Core average deviance explained (%)	# of layers: p-value ≤ 0.05		Parameter combinations	Core average deviance explained (%)	# of layers: p-value ≤ 0.05
Bq kg^{-1}				Bq m^{-2}			
All	water content + bulk density + elevation	53.56 (std. dev. 20.00)	5/14	All	water content + bulk density + elevation	43.58 (std. dev. 23.94)	5/14
Topo* only	slope degrees + plan curvature + TWI	40.62 (std. dev. 26.05)	0/14	Topo only	elevation + plan curvature + TWI	37.89 (std. dev. 23.40)	0/14
10 m DEM							
	Parameter combinations	Core average deviance explained (%)	# of layers: p-value ≤ 0.05		Parameter combinations	Core average deviance explained (%)	# of layers: p-value ≤ 0.05
Bq kg^{-1}				Bq m^{-2}			
All	water content + bulk density + elevation	54.03 (std. dev. 19.06)	6/14	All	water content + bulk density + elevation	44.09 (std. dev. 23.40)	414
Topo only	elevation + slope degrees + upslope distance	46.70 (std. dev. 26.02)	4/14	Topo only	elevation + slope degrees + upslope distance	41.83 (std. dev. 26.54)	4/14

*An abbreviation of "Topography".

Table 8 lists the most effective parameter combinations for explaining Cs-137 values. The rows are separated into combinations with all the parameters (including soil parameters) and combinations with only the topographic parameters. For both 1 m and 10 m DEMs, the most effective combinations were "water content + bulk density + elevation." When soil properties were removed, the most effective topographic parameter combinations were "slope degrees + plan curvature + TWI" when using the 1 m DEM and "elevation + slope degrees + upslope distance" when using the 10 m DEM. Overall, model performance was higher using the 10 m DEM and Cs-137 in Bq kg^{-1} units. The Cs-137 units made no difference in the best performance parameter combinations for each DEM resolution.

525 **6.3.4 GAM Prediction Results Validations**

No reference data were available to validate the model results. Therefore, Cs-137 levels were reverse-predicted using the two best performance models with the 10 m DEM from Table 8, and the model fits were checked. The "predict.gam()" function was used to make the prediction, and then the performance of the models was checked with the "gam.check ()" command. This command outputs several performance metrics of prediction fit. Figure 23 displays the check results for the two prediction
530 models. The output metrics are deviance-explained percentages, R^2, Akaike information criteria (AIC) for maximum likelihood (Eq. A4), and generalized cross-validation (GCV), which is the average ability of models fitted to the remaining data to predict the omitted data.

Higher deviance-explanation percentages and R^2 values indicate that a model performs well. Lower AIC indicates a good model with less information loss (parsimony), and lower GCV suggests a good model with a smaller prediction error (Hastie,
535 et al., 2009, Wood, 2017). The graphs in Fig. 24 show all four matrices' results by depth layer averages. The deviance-explained percentages and R^2 showed camelback-shaped fit changes across the depths. AIC and GCV decreased continuously.

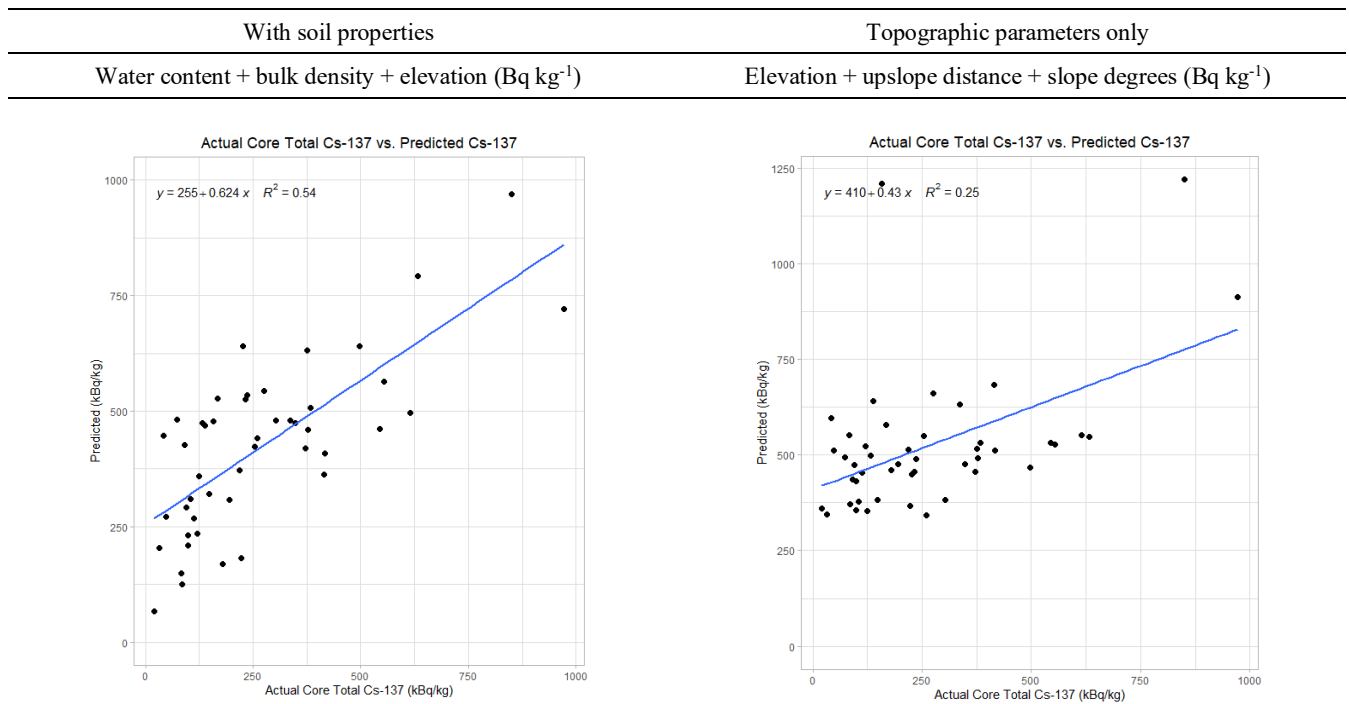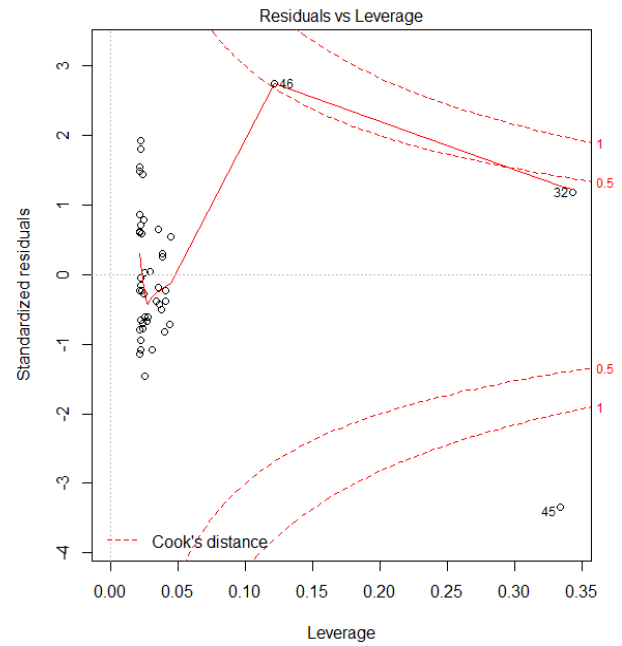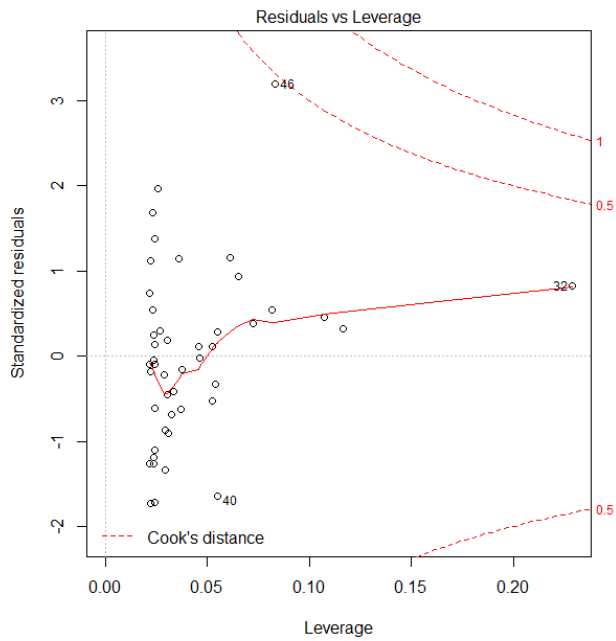| Soil properties and topographic parameters	Topographic parameters only
Water content + bulk density + elevation (Bq kg^{-1})	Elevation + upslope distance + slope degrees (Bq kg^{-1})

Figure 11. Model fit diagnosis results of the best-performing models using the 10 m DEM in Bq kg^{-1} unit (light gray: AIC; black: GCV score; dashed: deviance-explained percentage: loosely dash-dotted: R^2).

540

6.3.5 GAM prediction results validations: Outlier/influential sample analysis

Figure 24 presents linear regression scatterplots of actual Cs-137 values versus predicted Cs-137 values for the same two models. The model with soil properties returned a better model fit, with an R^2 of 0.54, compared to the model with only topographic parameters, which had an R^2 of 0.25. In the bottom graphs of Fig. 24, the y-axis is the Cook's distance and the x-axis is leverage (i.e., the measure of the extremity of a predictor). The red contours in the Cook's distance plots are standardized residual contours. The white circles, which are away from other sample groups, have a greater influence on the entire data distributions.

With soil properties	Topographic parameters only
Water content + bulk density + elevation (Bq kg^{-1})	Elevation + upslope distance + slope degrees (Bq kg^{-1})

Figure 12. Regression analysis of actual and predicted Cs-137 values and outliers (top row graphics: regression analysis; bottom row graphics: Cook's outliers).

These influential outlier samples are plotted in Fig. 25 with red circles over the flow direction map (left) and the winter vegetation map (right) of the study site. The locations of these outliners were spread on the west side hillslopes , and they were found in areas without evergreen vegetation (Fig. 25, right).
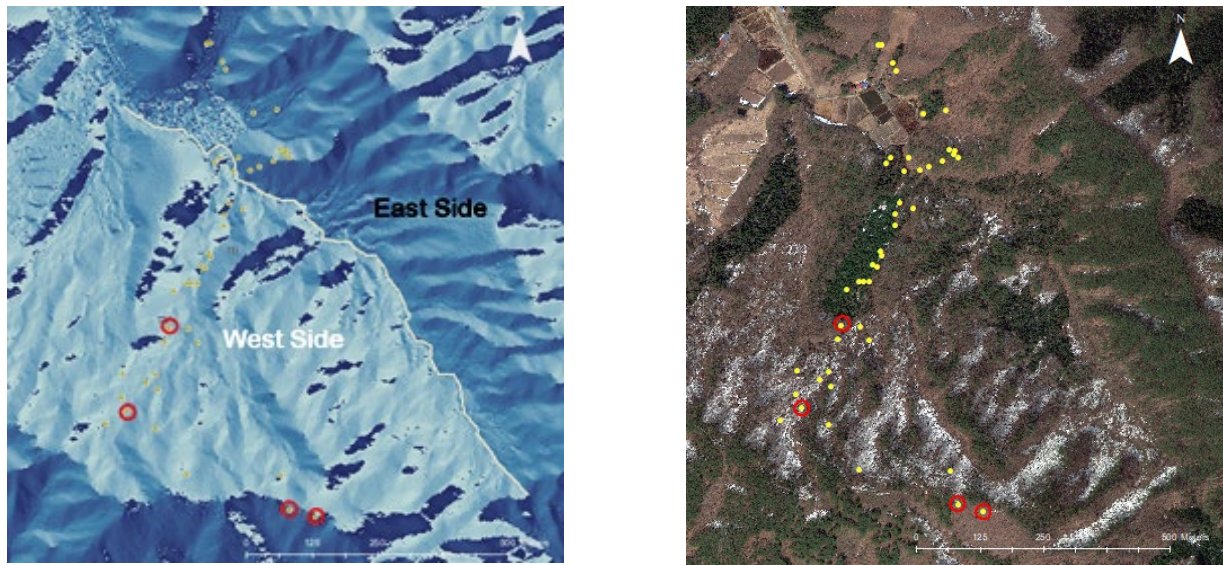
36

Figure 13. Cook's distance outlier samples overlaid on a flow direction map (left) and a winter vegetation image (right) (map data: © Google, Maxar Technologies). On the flow direction map, the cream line indicates the line where the surface flow converges into the main channel from the hillslopes on the opposite side.

560

6.4 Test 3 Results: Vegetation cover and hillslope aspects

To determine the significance of hillslope aspects and vegetation cover on the Cs-137 prediction results, an interaction term ("by=") was added to the GAM prediction models, and the models were run again. Both hillslope aspect and vegetation interaction terms had two categories: the east and west sides of a channel, and evergreen and deciduous vegetation cover
565 differences. Then, the mean differences in Cs-137 prediction results were checked pair-wise using a Tukey's HSD test. Each pair contained a combination of one parameter plus one categorical term on both sides (e.g., water content on the east side vs. elevation on the west side, elevation in the evergreen area vs. upslope distance in the deciduous area). The same paring was tested for all depth layers, and a confidence interval range was displayed for that pair.

570 Table 9 shows five pairs that returned significant mean differences. The results indicated that the pairs with topographic parameters returned considerable mean differences in Cs-137 predictions, particularly when the prediction results were sub-grouped by vegetation cover types. Among the topographic parameters, the slope degrees was the parameter that appeared to most affect the prediction results at the particular study site. side. According to Fig. 14, slope degrees increase along with an elevation increase; however, they influenced Cs-137 predictions in opposite ways.

575

Table 9. The parameter pairs that showed mean differences in the Tukey's HSD test for Cs-137 predictions (a 95 % confidence interval did not overlap the zero point)..

37

The parameter pairs returned significant mean differences					
water content	+	deciduous	vs.	elevation	+	evergreen
slope degrees	+	deciduous	vs.	elevation	+	deciduous
slope degrees	+	evergreen	vs.	elevation	+	deciduous
slope degrees	+	deciduous	vs.	upslope distance	+	evergreen
slope degrees	+	evergreen	vs.	upslope distance	+	evergreen

6.5 Test 4 Results: Spatial extrapolation test

580 In this section, using the GAM combinations with the best deviance-explained percentage, Cs-137 concentration in a basin (Fig. 5d) was extrapolated. According to Table 8, the most effective topographic parameter combination was "elevation + slope degrees + upslope distance" using the 10 m DEM in Bq kg^{-1} units. First, the extrapolation was tested with the original GAM prediction models for each depth layer. However, the spatially extrapolated Cs-137 values were overblown in some depth layers, returning unrealistically large concentration values. To resolve this issue, k=3 (wiggliness) was manually set to

585 constrain the model. The number of k= was increased incrementally; the resulting model performance and output plots were checked, and the number three was selected. By adding the k= term, the deviance explained percentage of the GAM model decreased from the core average 37.97 (original) to 33.84; and the p-value changed from 0.20 to 0.19.

The extrapolation result (Fig. 28) shows that the Cs-137 concentration in the basin was 3,158 MBq kg^{-1} (743 kBq m^{-2}) down to 30 cm deep as of 28 June 2016, assuming the dry bulk density to be 0.44 g cm^{-3}. Since this was an area-wide extrapolation,

590 the calculation for mass depth concentraiton was done by ([total Cs-137 (Bq kg^{-1})/ area (m^{-2})] × bulk density [kg m^{-3}] × depth [m]). When the concentration was decay-corrected, the prediction became 3,743 MBq kg^{-1} (880 kBq m^{-2}) for 15 March 2011. The estimated concentration was 12 % lower than the lowest end of the Japanese government's initial deposition estimate for the region (1,000–3,000 kBq m^{-2}; (MEXT, 2011). The total includes the pre-FDNPP accident background contamination and the estimated depositions in all raster cells, which include channels. The widths of the channels in the forest are about 30 cm

595 to 1 m. Thus, they were not separated in the 10 m resolution raster cells. The upper left (former rice paddy areas) and bottom right (lowland areas) corners of Fig. 28show white stripes because upslope distance and TWI did not return values in the flatlands. Figure 26 also shows the overlaid positions of Cook's outliers (red circles).

The extrapolated values in Bq kg^{-1} were overestimated toward higher values (+06 in the map legend; Fig. 28). The samples collected at the highest ridge in 2017 did contain a core total Cs-137 value of 0.97MBq kg^{-1} in average.Thes samples appeared

600 to have contributed to overestimation in the ridge areas. On the other hand, the calculated concentration in Bq m^{-2} was lower than the government's initial estimate. The average bulk density of the collected samples was 0.44 g cm^{-3}. But the actual average density at the study site soils might have been higher since most of the samples were collected at accessible locations – not at locations with steeper slope degrees (i.e., locations difficult to access with tools). In the areas with steep slope degrees,

soil density could have been higher. If the bulk density was 1.0g/cm^3, the Cs-137 concentration of the basin based on Bq kg^{-1}
would have been 1,688 kBq m^{-2} in 2016.
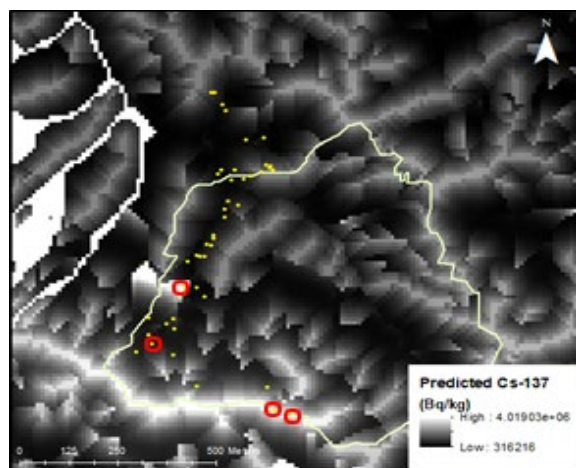
Figure 14. Extrapolated Cs-137 (Bq kg^{-1}) using "elevation + slope degrees + upslope distance." (White indicates higher concentration.) Red circles are the location of Cook's outliers.

7 Discussion

7.1 The effects of topography

Topographic effects on Cs-137 accumulation patterns are, by themselves, weak when a single parameter is used for Cs-137 prediction (deviance-explained percentages 3.83–28.31; Table 6). Elevation and slope degrees are commonly used in geomorphic assessment (Catani, et al., 2010, Chen, et al., 1997, Griffiths, et al., 2009, Hoover and Hursh, 1943, Roering, et al., 2001, Roering, 2008, Roering, et al., 1999, Rossi, et al., 2014, Yang, et al., 1998) and in Cs-137 contamination research (Ritchie and McHenry, 1990, Walling, et al., 1995). However, prediction models with only elevation or slope degrees explained Cs-137 concentrations at less than 28.31 % in either unit (Bq kg^{-1} or Bq m^{-2}).

The explanation power of water content and dry bulk density was higher (deviance explained percentages 17.93–36.16) (Table 7). When topographic parameters were combined among themselves or combined with soil property data, the GAM models' explanation powers improved (the best explanation percentages ranged from 37.89 % for a single-parameter model to 46.70 % for a mixed-parameter model; Table 8).

Despite the fact that slope degrees showed little significance for explaining Cs-137 as a single parameter, it was the most prevalent topographic parameter (Table 8) among the models with higher explanation percentages. The average minimum upslope distance from sampling points at the study site was 16.90 m with the 1 m DEM and 68.52 m with the 10 m DEM (Fig. 16), indicating that those hillslopes are composed of multiple small sub-basins with less than 100 m minimum upslopes. Hence,

in this particular case, elevation and slope alone could not efficiently explain all the Cs-137 concentration patterns. The camelback-shaped Cs-137 profiles on the representative hillslope (Fig. 13–Fig. 15) are the results of this spatial configuration.

7.2 Subsurface Migration

630 The vertical profiles of the GAM explanation percentages of soil properties and topographic parameters were similar throughout the depths (Fig. 18–Fig. 23), indicating that Cs-137 vertical profiles were the result of their co-functionalities. However, predictions solely with topographic parameters displayed wider ranges in those percentages and, for some samples, the models were unable to explain Cs-137 concentrations (gray dots closer to zero in Fig. 20 and Fig. 23).

Regarding Cs-137 accumulation on a sloped surface (Figures 14–16), it was generally assumed that: 1) Cs-137 accumulates at the bottom of the slope where surface runoffs converge, and 2) its accumulation levels are higher in lower slope-degree areas
635 where surface water pools. According Figure 16, the migration head depths were did not show a distinct trend along the elevation Considering that the migration head depths had already reached 30 cm deep in four of the samples, the actual trendlines in Figure 16 could have been tilted downwards at the lower elevations. Contrary to the assumptions, Cs-137 accumulation levels were lower at lower elevations (Figure 14), and the locations with higher Cs-137 accumulations or deeper migration head depths were not necessarily the locations with the lowest slope degrees (Fig. 15).

640 **Table 10. Comparison of Cs-137 downward migration depth between the CNPP accident–affected area and Fukushima at about the same length of time after the nuclear plant accidents.**

Ukraine, Belarus, Russia (Ivanov et al., 1997; 15 samples)			Current Study (Iitate Village, Fukushima, Japan; 58 samples)			
Depth of 90 % threshold of Cs-137 accumulation ($Bq\ cm^{-3}$)	Number and % of samples		Depth of 90 % threshold of Cs-137 accumulation ($Bq\ m^{-2}$)	Number and % of samples		
	Years passed 7	Years passed 8		Years passed 6	Years passed 7	Years passed 8
2 cm	1 (6.7 %)	1 (6.7 %)	2 cm			
4 cm	5 (33.3 %)	1 (6.7 %)	4 cm	8 (13.8 %)	1 (1.7 %)	11 (19.0 %)
6 cm	1 (6.7 %)	1 (6.7 %)	6 cm	4 (6.9 %)	1 (1.7 %)	4 (6.9 %)
7 cm	4 (26.7 %)		7 cm			
			8 cm	4 (6.9 %)	3 (5.2 %)	6 (10.3 %)
10 cm		1 (6.7 %)	10 cm	3 (5.2 %)	1 (1.7 %)	3 (5.2 %)
			12 cm	2 (3.4 %)		4 (6.9 %)
			14 cm	1 (1.7 %)		
			18 cm			1 (1.7 %)
			20 cm		1 (1.7 %)	

Table 10 compares the depths at which 90 % of the total Cs-137 concentration in soil samples was measured (not migration head depths). The results on the left are from a research paper published following the CNPP accident (Ivanov, et al., 1997).
645 The results on the right are from soil samples collected at the present study site. The numbers of samples and the years after

each respective accident differ between the two projects. However, the current study shows that Cs-137 migrated downward more quickly than in the region affected by the CNPP accident. The faster downward migration at the present study site may be attributed to the site's low bulk density of 0.44 g cm^{-3} and to its sandy soils.

650   According to Fig. 24, GAM models predicted well for the mid-depths, around 6.0 to 18.0 cm, which is important for mitigation purposes because the average migration head depth of the FDNPP-derived Cs-137 was 20.00 cm. The reasons why the model performance was poor in the depths of 2.0 to 6.0 cm (Fig. 18, Fig. 21, and Fig. 24) need further analysis, with more detailed soil property and the temporal change data of Cs-137 in the forest. The current assumption is that physical or biological factors that affect Cs-137 accumulation in those depths were not included in the models, such as the effects of Cs-137 migration from
655   surface litter and vegetation, organic matter in the soils, or infiltration patterns (see Sect. 7.4 below).

7.3 The effects of DEM resolutions

Overall, the topographic parameters extracted from the 10 m DEM returned higher explanation percentages than those extracted from the 1 m DEM (Tables 6 and 8). The results contradicted the authors' initial assumption that the 1 m DEM would capture the topography of the study site with microtopography. The descriptive statistics (Fig. 17) of the parameters showed
660   that TWI displayed the largest difference between the 1 m DEM and 10 m DEM. The median TWI with the 1 m DEM was 1.63 while, with the 10 m DEM, the corresponding TWI was 5.45. The parameter with the second-largest difference was upslope distance.

Upslope distance appeared in the best-performing parameter combinations for the 10 m DEM. The range of absolute plan
665   curvature values narrowed with the 10 m DEM, although the COV increased among the measurements (Fig. 16). (Heimsath, et al., 1999) have found that curvature becomes scale-dependent in grids larger than 5 m, supporting the reduced range of plan curvature values with the 10 m DEM in this study.

Table 11 lists each topographic parameter's median value ratios between the DEMs and with which DEM those parameters appeared in the better-performing models. These findings led the authors to two new hypotheses: (1) topographic features
670   appearing in the better-performing models with the 10 m DEM (elevation, upslope distance) had more effects on Cs-137 accumulation in a larger spatial scale than those parameters in the better-performing models with the 1 m DEM and (2) plan curvature and TWI (as already stated) reflected the physical processes in a spatial extent of less than 10 m.

Table 11. Difference ratios of DEM resolutions and the median measurements of topographic parameters.

Difference ratio	1 m DEM	10 m DEM	The DEM where each parameter appeared in the better-performing models
elevation	1.00	1.01	10 m DEM
slope degrees	1.08	1.00	1 m / 10 m DEM
upslope distance	1.00	4.05	10 m DEM
plan curvature	1.00	100.00	1 m DEM
TWI	1.00	3.34	1 m DEM

675

7.4 Soil Properties

Soil properties explained Cs-137 values in Bq kg^{-1} units at significant levels (p-values of 0.05 for water content and of 0.06 for bulk density as a core average p-value) (Table 7), confirming that Cs-137 accumulation in Bq kg^{-1} depends on soil texture and water content. For Cs-137 values in Bq m^{-2} units, the prediction performance with soil properties was less than Bq kg^{-1} units.

680　As mentioned in Sect. 7.2, the explanation percentages of models were higher in the mid-depths. Separate Pearson's correlation index analyses demonstrated that water content and Cs-137 values were correlated at depths between 6.0 and 22.5 cm (index average of 0.65 for Cs-137 in Bq kg^{-1}; 0.60 for Cs-137 in Bq m^{-2}). The correlation analyses also found that TWI was weekly correlated with Cs-137 at the depths (index average of 0.44 for Cs-137 in Bq kg^{-1}; 0.38 for Cs-137 in Bq m^{-2}). A hypothesis in this regard is that water content, resulting from infiltration and surface water pooling, has connections with Cs-137 levels and

685　helped GAM models predict Cs-137 concentrations in the mid-depths despite the large COVs of Cs-137 values at the same depths (Fig. 12–Fig. 13).

7.5 The Significance of vegetation cover types and hillslope aspects

The Tukey's HSD tests (Table 9) revealed the inter-effects of topography and vegetation cover types in predicting Cs-137 concentrations. When the samples were separated by evergreen and deciduous areas, the parameter pairs containing the

690　elevation, slope degrees, and upslope distance did make mean differences in the. At this particular study site, what matters for Cs-137 predictions was the combinations of topographic parameters centered on slope degrees – and the effects were enhanced by the vegetation growing on the slope. Hillslope aspects did not show significant differences in the predictions at this study site.

7.6 Model extrapolation performance

695　This study attempted a numerical spatial extrapolation using a model with only topographic parameters. The GAM model used for extrapolation ("elevation + slope degrees + upslope distance") had a deviance explanation percentage of less than 40 %,

and the model extrapolation result was 12 % less than the Japanese government's estimate; in other words, the model predicted up to 82 % of the lowest boundary of the expected total Cs-137 budget. The model needs to be improved by testing other topographic parameters and adding samples, if possible, in the future. Still, the extrapolation result was better than the numerical model suggested, and the result indicates the robustness of topographic parameters in geomorphological predictions.

8 Conclusions

This study examined and attempted to predict Cs-137 concentrations in a forest using a numerical approach. The study focused on the effects of topography on Cs-137 concentration levels and compared the effects of the soil properties. Generalized additive models (GAM) was used for the evaluation. The results showed that the combinations of topographic parameters affected the Cs-137 concentration levels; however, the explanation percentages were low. Combining multiple parameters returned better predictability. The comparison of the topographic parameters extracted from DEMs with different spatial resolutions showed the variabilities of parameter ranges, depending on the parameter extraction methods. Soil property data can enhance the performance of topography-based models for Cs-137 concentration predictions. However, the vertical results showed that topography and soil properties do not explain Cs-137 concentration consistently throughout the sampled soil depths. Although their relative prediction power was in sync in individual depth intervals, the degrees of explanation percentages themselves differed among the layers. Further analysis using mean differences in Cs-137 predictions revealed the inter-effects of topography and vegetation cover types in predicting Cs-137 concentrations. Lastly, the vertical migration speed of Cs-137 in the Fukushima forest was faster than the corresponding speed in the area affected by the CNPP accident. The final extrapolation attempt demonstrated the possibility of predicting radionuclide contamination based on topographic features. These results provide consideration points to environmental radioactivity research that investigates the contamination patterns in a particular topography. As an environmental tracer, Cs-137 can be used to as a tool to understand the subsurface inter-functionality of topography, surface hydrology, and soil properties, not only for tracking surface soil translocation.

9 Limitations

9.1 Comments on temporal dynamics

In this study, Cs-137 measurement began in 2016, and the physical translocation of Cs-137 prior to 2016 was not considered. The physical processes that might have affected Cs-137 movements before 2016 is a black box; prior to 2016, no soil monitoring was conducted in the study-site forests. The only data the authors had were the initial Cs-137 deposition estimate for the study site region by the Japanese government and the United States Department of Defense (MEXT, 2011). Cs-137 values are decay-normalized in this article, and thus, the research does not consider the physical translocation of Cs-137 over the three-year sampling period. Channel discharge Cs-137 data, which would have provided a clue on surface Cs-137 loss at the study site over the years, also does not exist. Considering that the average soil bulk density was 0.44g/cm^3, which is a very

low dry bulk density, the extent of Cs-137 loss due to surface runoff was considered to be limited (Bharati, et al., 2002, Meek, et al., 1992). However, the effects of constant precipitation in rainy seasons, as well as the intense typhoon season precipitation in Japan, cannot be ignored. Still, all soil sampling campaigns were conducted at approximately the same time of year during all three data collection years – after the end of the rainy season in Japan. All sampling campaigns avoided intense precipitation immediately prior to sample collections. Thus, the ground and soil conditions did not differ significantly.

The authors conducted a separate temporal investigation of changes between the 2016 and 2018 samples. This investigation showed that the average COG depth among samples moved down less than 1.0 cm and the average migration head depth moved up 1.75 cm between the two years. Although there were variations among the samples, the overall Cs-137 vertical accumulation patterns in the soils did not change drastically over two years. These temporal changes will be addressed in a separate article.

9.2 Other Limitations

1) The results of this research apply only to the study site, but the analytical methods can be applied to other sites. Whether the same topographic factors significantly affect Cs-137 must be verified in other locations.

2) The importance of organic matter in understanding Cs-137 behavior has been recognized (Claverie, et al., 2019, Doerr and Münnich, 1989, Dumat, et al., 1997, Dumat, et al., 2000, Fan, et al., 2014, Korobova, et al., 2016, Mabit, et al., 2008, Staunton, et al., 2002, Takenaka, et al., 1998, Tatsuno, et al., 2020), and carbon/nitrogen (C/N) ratio measurement for the collected samples was attempted in 2016. However, due to time constraints and equipment issues, data were extracted for only a small portion of the samples. Research using soils from the same forest (Tatsuno, et al., 2020) has reported the effects of dissolved organic matter on Cs transport. The authors, therefore, refer readers interested in the topic to Tatsuno et al. (2020).

Author contributions

Yasumiishi, M. conceived and designed the project; Yasumiishi, M. and Nishimura, T. conducted field data collections and laboratory analysis; Yasumiishi, M. conducted data analysis and graphing; Nishimura, T., Aldstadt, J., and Bennett, SJ. Provided critical feedback on data analysis; Yasumiishi, M. drafted the manuscript; Bittner, T. advised on data concepts. All authors provided critical feedback to finalize the manuscript.

Competing interests

The authors declare that they have no conflict of interest.

Acknowledgments

Appendices

Appendix A. The standard setting for GAM models.

Model ← gam(Cs-137 ~ s(x_1) + s(x_2) + s(x_3), data=data, method="REML", bs="cr", family=Gamma(link=log)),

where s indicates that the spline-based smooth term is applied to the variable; bs sets the (penalized) smoothing basis; REML indicates restricted maximum likelihood; and cr indicates that cubic splines are used. This GAM setting was consistent for all model runs.

Appendix B. The GAM model setting with a categorical term.

Model ← gam(Cs-137 ~ Vegetation Type/Location + s(x_1) + s(x_1, by=Vegetation Type/Location, m=1) + s(x_2) + s(x_3), data=data, method="REML", bs="cr", family=gamma (link=identity))

The x_1 variable was evaluated by itself and then with the subcategories. The "m=1" term ensured that the model put the penalty on the first derivative for the difference smooths. The "by=" term was applied to each variable in the GAM equation, one at a time.

Appendix C. Generalized cross-validation (GCV) equation.

$$V_g = \frac{\sum_{i=1}^{n} n(y_i - \hat{f}_i)^2}{[n - \text{tr}(A)]^2} \text{ (Wood, 2017)} \tag{A1},$$

where V_g is the generalized cross-validation score, y_i is the excluded data, $\hat{f}$ is the estimate from fitting to all the data, and tr(A) is the mean of the model matrix A_{ii}.

Appendix D. Cs-137 decay equation.

The Cs-137 decay constant is calculated as follows (Eq. A1):

$$\lambda = \frac{\ln 2}{T_{\frac{1}{2}}} \tag{A2},$$

785 where λ is the decay constant and $T_{1/2}$ is the half-life. The half-life of Cs-137 is 30.17 years; thus, $\lambda = 0.022975$ year^{-1}. The radioactive decay formula is as follows (Eq. A2):

$$N_0 = \frac{Nt}{e - \lambda t} \tag{A3},$$

where N_0 is the original Cs-137 value, Nt is the Cs-137 value after time t, and λ is the decay constant (IAEA-TECDOC, 2003).

Appendix E. Akaike information criteria (AIC) equation.

790 $AIC = -2l(\hat{\theta}) + 2p$ (Wood, 2017) $\tag{A4},$

where $l(\hat{\theta})$ is log-likelihood and p is the number of identifiable model parameters (usually, the dimension of θ).

References

Amaral, E., Amundsen, I., Barišić, D., Booth, P., Clark, D., Ditmars, J., Dlouhy, Z., Drury, N., Gehrche, K. and Gnugnoli, G.:
795   Characterization of radioactively contaminated sites for remediation purposes, IAEA-Tecdoc, 1017, 1-103, 1998.

Barker, R. J., Van Den Bussche, R. A., Wright, A. J., Wiggins, L. E., Hamilton, M. J., Reat, E. P., Smith, M. H., Lomakin, M. D. and Chesser, R. K.: High levels of genetic change in rodents of Chernobyl, Nature, 380, 6576, 707, 1996.

Bennett, S. J., Rhoton, F. E. and Dunbar, J. A.: Texture, spatial distribution, and rate of reservoir sedimentation within a highly erosive, cultivated watershed: Grenada Lake, Mississippi, Water resources research, 41, 1, doi:10.1029/2004wr003645, 2005.

800   Bharati, L., Lee, K.-H., Isenhart, T. and Schultz, R.: Soil-water infiltration under crops, pasture, and established riparian buffer in Midwestern USA, Agroforestry systems, 56, 3, 249-257, doi:10.1023/A:1021344807285, 2002.

Burr, T. and Hamada, M.: Radio-Isotope Identification Algorithms for NaI γ Spectra, Algorithms, 2, 1, 339-360, doi:10.3390/a2010339, 2009.

Catani, F., Segoni, S. and Falorni, G.: An empirical geomorphology-based approach to the spatial prediction of soil thickness
805   at catchment scale, Water Resources Research, 46, 5, doi:10.1029/2008wr007450, 2010.

Chen, Z.-S., Hsieh, C.-F., Jiang, F.-Y., Hsieh, T.-H. and Sun, I.-F.: Relations of soil properties to topography and vegetation in a subtropical rain forest in southern Taiwan, Plant Ecology, 132, 2, 229-241, doi:10.1023/A:1009762704553, 1997.

Clark, M.: Generalized additive models: getting started with additive models in R, Center for Social Research, University of Notre Dame, 35, 2013.

810   Claverie, M., Garcia, J., Prevost, T., Brendlé, J. and Limousy, L.: Inorganic and Hybrid (Organic–Inorganic) Lamellar Materials for Heavy Metals and Radionuclides Capture in Energy Wastes Management—A Review, Materials, 12, 9, 1399, doi:10.3390/ma12091399, 2019.

Climate-Data.Org: Prypiat Climate https://en.climate-data.org/europe/ukraine/kyiv-oblast/prypiat-715182/, Last Accessed: Nov 25, 2019.

815   Cook, R. D.: Detection of influential observation in linear regression, Technometrics, 19, 1, 15-18, doi:10.2307/1268249, 1977.

Coughtrey, P., Kirton, J., Mitchell, N. and Morris, C.: Transfer of radioactive caesium from soil to vegetation and comparison with potassium in upland grasslands, Environmental Pollution, 62, 4, 281-315, doi:10.1016/0269-7491(89)90150-4, 1989.

Davis, S.: Screening For Thyroid Cancer after the Fukushima Disaster: What Do We Learn From Such An Effort?,
820   Epidemiology, doi:10.1097/EDE.0000000000000397, 2016.

Doerr, H. and Münnich, K.: Downward movement of soil organic matter and its influence on trace-element transport (210Pb, 137Cs) in the soil, Radiocarbon, 31, 3, 655-663, doi:10.1017/s003382220001225x, 1989.

Dumat, C., Cheshire, M., Fraser, A., Shand, C. and Staunton, S.: The effect of removal of soil organic matter and iron on the adsorption of radiocaesium, European Journal of Soil Science, 48, 4, 675-683, doi:10.1111/j.1365-2389.1997.tb00567.x, 1997.

825   Dumat, C., Quiquampoix, H. and Staunton, S.: Adsorption of cesium by synthetic clay− organic matter complexes: effect of the nature of organic polymers, Environmental science & technology, 34, 14, 2985-2989, doi:10.1021/es990657o, 2000.

EPA: Radiological Laboratory Sample Analysis Guide for Incident Response – Radionuclides in Soil, 2012.

Fan, Q., Tanaka, M., Tanaka, K., Sakaguchi, A. and Takahashi, Y.: An EXAFS study on the effects of natural organic matter and the expandability of clay minerals on cesium adsorption and mobility, Geochimica et Cosmochimica Acta, 135, 49-65,
830   doi:10.1016/j.gca.2014.02.049, 2014.

Fesenko, S. V., Alexakhin, R. M., Balonov, M. I., Bogdevitch, I. M., Howard, B. J., Kashparov, V. A., Sanzharova, N. I., Panov, A. V., Voigt, G. and Zhuchenka, Y. M.: An extended critical review of twenty years of countermeasures used in agriculture after the Chernobyl accident, Science of the total environment, 383, 1, 1-24, doi:10.1016/j.scitotenv.2007.05.011, 2007.

835   Fujii, K., Ikeda, S., Akama, A., Komatsu, M., Takahashi, M. and Kaneko, S.: Vertical migration of radiocesium and clay mineral composition in five forest soils contaminated by the Fukushima nuclear accident, Soil science and plant nutrition, 60, 6, 751-764, doi:10.1080/00380768.2014.926781, 2014.

Gallant, J. C. and Wilson, J. P.: TAPES-G: a grid-based terrain analysis program for the environmental sciences, Computers & Geosciences, 22, 7, 713-722, doi:10.1016/0098-3004(96)00002-7, 1996.

840 Gellis, A. and Walling, D.: Sediment source fingerprinting (tracing) and sediment budgets as tools in targeting river and watershed restoration programs, Stream restoration in dynamic fluvial systems: scientific approaches, analyses, and tools, 194, 263-291, doi:10.1029/2010GM000960, 2011.

Gessler, P. E., Moore, I., McKenzie, N. and Ryan, P.: Soil-landscape modelling and spatial prediction of soil attributes, International Journal of Geographical Information Systems, 9, 4, 421-432, doi:10.1080/02693799508902047, 1995.

845 Griffiths, R. P., Madritch, M. D. and Swanson, A. K.: The effects of topography on forest soil characteristics in the Oregon Cascade Mountains (USA): Implications for the effects of climate change on soil properties, Forest Ecology and Management, 257, 1, 1-7, doi:10.1016/j.foreco.2008.08.010, 2009.

Hashimoto, S., Matsuura, T., Nanko, K., Linkov, I., Shaw, G. and Kaneko, S.: Predicted spatio-temporal dynamics of radiocesium deposited onto forests following the Fukushima nuclear accident, Scientific reports, 3, doi:10.1038/srep02564,
850 2013.

Hashimoto, S., Ugawa, S., Nanko, K. and Shichi, K.: The total amounts of radioactively contaminated materials in forests in Fukushima, Japan, Scientific reports, 2, 416, doi:10.1038/srep00416, 2012.

Hastie, T., Tibshirani, R. and Friedman, J.: The elements of statistical learning: data mining, inference, and prediction, Springer Science & Business Media, 2009.

855 Heimsath, A., Dietrich, W., Nishiizumi, K. and Finkel, R.: The soil production function and landscape equilibrium, Nature, 388, 6640, 358, doi:10.1038/41056, 1997.

Heimsath, A. M., Dietrich, W. E., Nishiizumi, K. and Finkel, R. C.: Cosmogenic nuclides, topography, and the spatial variation of soil depth, Geomorphology, 27, 1-2, 151-172, doi:10.1016/s0169-555x(98)00095-6, 1999.

Hengl, T. and Reuter, H. I.: Geomorphometry: concepts, software, applications, Newnes, 2008.

860 Hoover, M. and Hursh, C.: Influence of topography and soil-depth on runoff from forest land, Eos, Transactions American Geophysical Union, 24, 2, 693-698, doi:10.1029/tr024i002p00693, 1943.

IAEA-TECDOC: 1340: Manual for reactor produced radioisotopes, Vienna: International Atomic Energy Agency, 2003.

IAEA: Use of isotope and radiation methods in soil and water management and crop nutrition, 2001.

IAEA: Fukushima Daiichi Accident Technical Volume 4/5 Radiological Consequences, 2015.

865 IAEA: Guidelines on Soil and Vegetation Sampling for Radiological Monitoring, Technical Reports Series, 2019.

IAEA: Case Study on Assessment of Radiological Environmental Impact from Potential Exposure, Vienna, INTERNATIONAL ATOMIC ENERGY AGENCY, 2020.

IAEA and INES: The international nuclear and radiological event scale, Information Series, International Atomic Energy Agency, Vienna, Austria, 4, 2008.

870 Istanbulluoglu, E., Yetemen, O., Vivoni, E. R., Gutiérrez-Jurado, H. A. and Bras, R. L.: Eco-geomorphic implications of hillslope aspect: Inferences from analysis of landscape morphology in central New Mexico, Geophysical Research Letters, 35, 14, doi:10.1029/2008GL034477, 2008.

Ivanov, Y. A., Lewyckyj, N., Levchuk, S., Prister, B., Firsakova, S., Arkhipov, N., Arkhipov, A., Kruglov, S., Alexakhin, R. and Sandalls, J.: Migration of 137Cs and 90Sr from Chernobyl fallout in Ukrainian, Belarussian and Russian soils, Journal of
875 Environmental Radioactivity, 35, 1, 1-21, doi:10.1016/s0265-931x(96)00036-7, 1997.

Iwagami, S., Tsujimura, M., Onda, Y., Nishino, M., Konuma, R., Abe, Y., Hada, M., Pun, I., Sakaguchi, A. and Kondo, H.: Temporal changes in dissolved 137 Cs concentrations in groundwater and stream water in Fukushima after the Fukushima Dai-ichi Nuclear Power Plant accident, Journal of environmental radioactivity, doi:10.1016/j.jenvrad.2015.03.025, 2015.

Japan Forest Agency: The ares of natural and planted forests by prefectures,
880 https://www.rinya.maff.go.jp/j/keikaku/genkyou/h29/1.html, Last Accessed: June 26, 2017.

Japan Meteorological Agency: Data and References, http://www.jma.go.jp/jma/menu/menureport.html, Last Accessed: September 2, 2019.

Kato, H., Onda, Y. and Teramage, M.: Depth distribution of 137 Cs, 134 Cs, and 131 I in soil profile after Fukushima Dai-ichi Nuclear Power Plant accident, Journal of Environmental Radioactivity, 111, 59-64, doi:10.1016/j.jenvrad.2011.10.003, 2012.

885 Kim, S. and Lee, H.: A digital elevation analysis: a spatially distributed flow apportioning algorithm, Hydrological Processes, 18, 10, 1777-1794, doi:10.1002/hyp.1446, 2004.

Koarashi, J., Atarashi-Andoh, M., Matsunaga, T., Sato, T., Nagao, S. and Nagai, H.: Factors affecting vertical distribution of Fukushima accident-derived radiocesium in soil under different land-use conditions, Science of the Total Environment, 431, 392-401, doi:10.1016/j.scitotenv.2012.05.041, 2012.

890   Komamura, M., Tsumura, A., Yamaguchi, N., Fujiwara, E., Konokata, N. and Kodaira, K.: わが国の米, 小麦および土壌における 90Sr と 137Cs 濃度の長期モニタリングと変動解析, 農業環境技術研究所報告, 24, 1-21, 2006.

Komissarov, M. and Ogura, S.: Distribution and migration of radiocesium in sloping landscapes three years after the Fukushima-1 nuclear accident, Eurasian Soil Science, 50, 7, 861-871, doi:10.1134/s1064229317070043, 2017.

Korobova, E., Anoshko, Y., Kesminiene, A., Kouvyline, A., Romanov, S., Tenet, V., Suonio, E. and Cardis, E.: Evaluation of
895   stable iodine status of the areas affected by the Chernobyl accident in an epidemiological study in Belarus and the Russian Federation, Journal of Geochemical Exploration, 107, 2, 124-135, 2010.

Korobova, E., Ermakov, A. and Linnik, V.: 137 Cs and 90 Sr mobility in soils and transfer in soil–plant systems in the Novozybkov district affected by the Chernobyl accident, Applied Geochemistry, 13, 7, 803-814, 1998.

Korobova, E. and Romanov, S.: A Chernobyl 137Cs contamination study as an example for the spatial structure of geochemical
900   fields and modeling of the geochemical field structure, Chemometrics and Intelligent Laboratory Systems, 99, 1, 1-8, doi:10.1016/j.chemolab.2009.07.009, 2009.

Korobova, E. and Romanov, S.: Experience of mapping spatial structure of Cs-137 in natural landscape and patterns of its distribution in soil toposequence, Journal of Geochemical Exploration, 109, 1-3, 139-145, doi:10.1016/j.gexplo.2011.02.006, 2011.

905   Korobova, E., Romanov, S., Baranchukov, V., Berezkin, V., Korotkov, A. and Dogadkin, N.: Specificity of the 137Cs distribution in arable elementary landscape-geochemical system contaminated during the accident at the Chernobyl NPP, Applied Geochemistry, 104394, doi:10.1016/j.apgeochem.2019.104394, 2019.

Korobova, E. M., Brown, J. B., Ukraintseva, N. G. and Surkov, V. V.: 137 Cs and 40 K in the terrestrial vegetation of the Yenisey Estuary: landscape, soil and plant relationships, Journal of environmental radioactivity, 96, 1, 144-156,
910   doi:10.1016/j.jenvrad.2007.01.024, 2007.

Korobova, E. M., Linnik, V. G. and Brown, J.: Distribution of artificial radioisotopes in granulometric and organic fractions of alluvial soils downstream from the Krasnoyarsk Mining and Chemical Combine (KMCC), Russia, Journal of soils and sediments, 16, 4, 1279-1287, doi:10.1007/s11368-015-1268-2, 2016.

Kovalchuk, O., Arkhipov, A., Barylyak, I., Karachov, I., Titov, V., Hohn, B. and Kovalchuk, I.: Plants experiencing chronic
915   internal exposure to ionizing radiation exhibit higher frequency of homologous recombination than acutely irradiated plants, Mutation Research/Fundamental and Molecular Mechanisms of Mutagenesis, 449, 1, 47-56, 2000.

Linnik, V. G., Korobova, E. M. and Brown, J. E.: A historical outline of radionuclide contamination of the Yenisey floodplain based on landscape and radiometric survey, ENVIRONMENT SUSTAINABILITY, 2013.

Linnik, V. G., Saveliev, A. A. and Sokolov, A. V.: Transformation of the Chernobyl 137 Cs Contamination Patterns at the
920   Microlandscape Level as an Indicator of Stochastic Landscape Organization, Landscape Patterns in a Range of Spatio-Temporal Scales, Springer, 77-89,2020.

Linnik Vitaly, R. A. o. S.: Landscape Differentiation of Technogenic Radionuclides 372, 2018.

Loughran, R., Campbell, B. and Walling, D.: Soil erosion and sedimentation indicated by caesium 137: Jackmoor Brook catchment, Devon, England, Catena, 14, 1-3, 201-212, doi:10.1016/s0341-8162(87)80018-8, 1987.

925   Lowrance, R., McIntyre, S. and Lance, C.: Erosion and deposition in a field/forest system estimated using cesium-137 activity, Journal of soil and water conservation, 43, 2, 195-199, 1988.

Mabit, L., Bernard, C. and Laverdière, M. R.: Assessment of erosion in the Boyer River watershed (Canada) using a GIS oriented sampling strategy and 137Cs measurements, Catena, 71, 2, 242-249, doi:10.1016/j.catena.2006.02.011, 2007.

Mabit, L., Bernard, C., Makhlouf, M. and Laverdière, M.: Spatial variability of erosion and soil organic matter content
930   estimated from 137Cs measurements and geostatistics, Geoderma, 145, 3-4, 245-251, doi:10.1016/j.geoderma.2008.03.013, 2008.

Mahaffey, J.: Atomic Accidents: A History of Nuclear Meltdowns and Disasters: from the Ozark Mountains to Fukushima, Open Road Media, 2014.

Mahara, Y.: Storage and migration of fallout strontium-90 and cesium-137 for over 40 years in the surface soil of Nagasaki,
935   Journal of Environmental quality, 22, 4, 722-730, doi:10.2134/jeq1993.00472425002200040013x, 1993.

Martin, Y.: Modelling hillslope evolution: linear and nonlinear transport relations, Geomorphology, 34, 1-2, 1-21, doi:10.1016/s0169-555x(99)00127-0, 2000.

Martz, L. and De Jong, E.: Using Cesium-137 to assess the variability of net soil erosion and its association with topography in a Canadian prairie landscape, Catena, 14, 5, 439-451, doi:10.1016/0341-8162(87)90014-2, 1987.

940　Matsunaga, T., Koarashi, J., Atarashi-Andoh, M., Nagao, S., Sato, T. and Nagai, H.: Comparison of the vertical distributions of Fukushima nuclear accident radiocesium in soil before and after the first rainy season, with physicochemical and mineralogical interpretations, Science of the total environment, 447, 301-314, doi:10.1016/j.scitotenv.2012.12.087, 2013.

Meek, B. D., Rechel, E., Carter, L. M., DeTar, W. R. and Urie, A.: Infiltration rate of a sandy loam soil: effects of traffic, tillage, and plant roots, Soil Science Society of America Journal, 56, 3, 908-913, 945　doi:10.2136/sssaj1992.03615995005600030038x, 1992.

MEXT, J.: 第 48 回環境放射能調査研究 成果論文抄録集, Ministry of Education, Culture, Sports, Science and Technology, Japan, 2006.

MEXT, J.: 文部科学省による放射線量等分布マップ (放射性セシウムの土壌濃度マップ) の作成について, http://radioactivity. mext. go. jp/ja/ontents/6000/5043/24/11555_0830. pdf, 2011.

950　Ministry of Agriculture Forestry and Fisheries: Annual Report on Forest and Forestry in Japan, 2013.

Miyahara, K. A., T; Kohara, Y; Yusa, Y; Sasaki, N: Effect of bulk density on diffusion for cesium in compacted sodium bentonite, Radiochimica Acta, 52, 2, 293-298, doi:10.1524/ract.1991.5253.2.293, 1991.

Møller, A. P. and Mousseau, T. A.: Biological consequences of Chernobyl: 20 years on, Trends in ecology & evolution, 21, 4, 200-207, doi:10.1016/j.tree.2006.01.008 2006.

955　Momm, H. G., Bingner, R. L., Wells, R. R. and Wilcox, D.: AGNPS GIS-based tool for watershed-scale identification and mapping of cropland potential ephemeral gullies, Applied engineering in agriculture, 28, 1, 17-29, doi:10.13031/2013.41282, 2012.

Moore, I., Burch, G. and Mackenzie, D.: Topographic effects on the distribution of surface soil water and the location of ephemeral gullies, Transactions of the ASAE, 31, 4, 1098-1107, 1988.

960　Moore, I. D., Gessler, P., Nielsen, G. and Peterson, G.: Soil attribute prediction using terrain analysis, Soil Science Society of America Journal, 57, 2, 443-452, doi:10.2136/sssaj1993.03615995005700020026x, 1993.

Murota, K., Saito, T. and Tanaka, S.: Desorption kinetics of cesium from Fukushima soils, Journal of environmental radioactivity, 153, 134-140, doi:10.1016/j.jenvrad.2015.12.013, 2016.

Nagao, S.: Radionuclides released from nuclear accidents: Distribution and dynamics in soil, Environmental Remediation 965　Technologies for Metal-Contaminated Soils, Springer, 43-65,2016.

Nakao, A., Thiry, Y., Funakawa, S. and Kosaki, T.: Characterization of the frayed edge site of micaceous minerals in soil clays influenced by different pedogenetic conditions in Japan and northern Thailand, Soil science and plant nutrition, 54, 4, 479-489, doi:10.1111/j.1747-0765.2008.00262.x, 2008.

Nobori, T., Tanoi, K. and Nakanishi, T.: オートサンプラー付き NaI (Tl) シンチレーションカウンターによる土壌およ 970　び作物中の放射性セシウム測定, Japanese Journal of Soil Science and Plant Nutrition, 84, 3, 182-186, 2013.

Ohnuki, T. and Kozai, N.: Adsorption behavior of radioactive cesium by non-mica minerals, Journal of Nuclear Science and Technology, 50, 4, 369-375, doi:10.1080/00223131.2013.773164, 2013.

Onda, Y., Kato, H., Hoshi, M., Takahashi, Y. and Nguyen, M.-L.: Soil sampling and analytical strategies for mapping fallout in nuclear emergencies based on the Fukushima Dai-ichi Nuclear Power Plant accident, Journal of environmental radioactivity, 975　139, 300-307, doi:10.1016/j.jenvrad.2014.06.002 2015.

Osawa, K., Nonaka, Y., Nishimura, T., Tanoi, K., Matsui, H., Mizogichi, M. and Tatsuno, T.: Quantification of dissolved and particulate radiocesium fluxes in two rivers draining the main radioactive pollution plume in Fukushima, Japan (2013–2016), Anthropocene, 22, 40-50, doi:10.1016/j.ancene.2018.04.003, 2018.

Park, S.-M., Alessi, D. S. and Baek, K.: Selective adsorption and irreversible fixation behavior of cesium onto 2: 1 layered 980　clay mineral: A mini review, Journal of hazardous materials, 369, 569-576, doi:10.1016/j.jhazmat.2019.02.061, 2019.

Pennock, D., Jong, E. d. and Lemmen, D.: Cesium-137-measured erosion rates for soils of five parent-material groups in southwestern Saskatchewan, Canadian Journal of Soil Science, 75, 2, 205-210, doi:10.4141/cjss95-028, 1995.

Quine, T. A., Govers, G., Walling, D. E., Zhang, X., Desmet, P. J., Zhang, Y. and Vandaele, K.: Erosion processes and landform evolution on agricultural land—new perspectives from caesium-137 measurements and topographic-based erosion 985　modelling, Earth Surface Processes and Landforms: The Journal of the British Geomorphological Group, 22, 9, 799-816, doi:10.1002/(sici)1096-9837(199709)22:9<799::aid-esp765>3.0.co;2-r, 1997.

Quinn, P., Beven, K., Chevallier, P. and Planchon, O.: The prediction of hillslope flow paths for distributed hydrological modelling using digital terrain models, Hydrological processes, 5, 1, 59-79, doi:10.1002/hyp.3360050106, 1991.

Quinn, P., Beven, K. and Lamb, R.: The in (a/tan/β) index: How to calculate it and how to use it within the topmodel framework, Hydrological processes, 9, 2, 161-182, doi:10.1002/hyp.3360090204, 1995.

R Core Team: R Foundation for Statistical Computing; Vienna, Austria: 2014, R: A language and environment for statistical computing, 2013, 2015.

Ritchie, J. and Ritchie, C.: 137 Cs use in erosion and sediment deposition studies: Promises and problems, 1995.

Ritchie, J. C. and McHenry, J. R.: Application of radioactive fallout cesium-137 for measuring soil erosion and sediment accumulation rates and patterns: a review, Journal of environmental quality, 19, 2, 215-233, doi:10.2134/jeq1990.00472425001900020006x, 1990.

Roering, J., Kirchner, J. and Dietrich, W.: Hillslope evolution by nonlinear, slope-dependent transport: Steady state morphology and equilibrium adjustment timescales, Journal of Geophysical Research: Solid Earth, 106, B8, 16499-16513, doi:10.1029/2001jb000323 2001.

Roering, J. J.: How well can hillslope evolution models "explain" topography? Simulating soil transport and production with high-resolution topographic data, Geological Society of America Bulletin, 120, 9-10, 1248-1262, doi:10.1130/B26283.1, 2008.

Roering, J. J., Kirchner, J. W. and Dietrich, W. E.: Evidence for nonlinear, diffusive sediment transport on hillslopes and implications for landscape morphology, Water Resources Research, 35, 3, 853-870, doi:10.1029/1998wr900090, 1999.

Rosén, K., Öborn, I. and Lönsjö, H.: Migration of radiocaesium in Swedish soil profiles after the Chernobyl accident, 1987–1995, Journal of Environmental Radioactivity, 46, 1, 45-66, doi:10.1016/s0265-931x(99)00040-5, 1999.

Rossi, G., Ferrarini, A., Dowgiallo, G., Carton, A., Gentili, R. and Tomaselli, M.: Detecting complex relations among vegetation, soil and geomorphology. An in-depth method applied to a case study in the Apennines (Italy), Ecological Complexity, 17, 87-98, doi:10.1016/j.ecocom.2013.11.002, 2014.

Sakuma, K., Tsuji, H., Hayashi, S., Funaki, H., Malins, A., Yoshimura, K., Kurikami, H., Kitamura, A., Iijima, K. and Hosomi, M.: Applicability of Kd for modelling dissolved 137Cs concentrations in Fukushima river water: Case study of the upstream Ota River, Journal of environmental radioactivity, 184, 53-62, doi:10.1016/j.jenvrad.2018.01.001, 2018.

Schimmack, W., Bunzl, K., Dietl, F. and Klotz, D.: Infiltration of radionuclides with low mobility (137Cs and 60Co) into a forest soil. Effect of the irrigation intensity, Journal of environmental radioactivity, 24, 1, 53-63, doi:10.1016/0265-931x(94)90024-8 1994.

Schimmack, W., Bunzl, K. and Zelles, L.: Initial rates of migration of radionuclides from the Chernobyl fallout in undisturbed soils, Geoderma, 44, 2-3, 211-218, doi:10.1016/0016-7061(89)90030-x 1989.

Scott, B. R.: Health risks from high-level radiation exposures from radiological weapons, Radiat Prot Manage, 21, 6, 9-25, 2004.

Shiozawa, S., Tanoi, K., Nemoto, K., Yoshida, S., Nishida, K., Hashimoto, K., Sakurai, K., Nakanishi, T. M., Nihei, N. and Ono, Y.: Vertical concentration profiles of radioactive caesium and convective velocity in soil in paddy field in Fukushima, Radioisotopes (Tokyo), 60, 8, 323-328, doi:10.3769/radioisotopes.60.323 2011.

Staunton, S., Dumat, C. and Zsolnay, A.: Possible role of organic matter in radiocaesium adsorption in soils, Journal of Environmental Radioactivity, 58, 2, 163-173, doi:10.1016/s0265-931x(01)00064-9 2002.

Stevens, J. P.: Outliers and influential data points in regression analysis, Psychological Bulletin, 95, 2, 342, 1984.

Stinnett, J. and Sullivan, C. J.: An automated isotope identification algorithm using Bayesian statistics,2013 IEEE Nuclear Science Symposium and Medical Imaging Conference (2013 NSS/MIC), 2013, IEEE, 1-7

Takahashi, J., Tamura, K., Suda, T., Matsumura, R. and Onda, Y.: Vertical distribution and temporal changes of 137Cs in soil profiles under various land uses after the Fukushima Dai-ichi Nuclear Power Plant accident, Journal of environmental radioactivity, 139, 351-361, doi:10.1016/j.jenvrad.2014.07.004 2015.

Takenaka, C., Onda, Y. and Hamajima, Y.: Distribution of cesium-137 in Japanese forest soils: Correlation with the contents of organic carbon, Science of the total environment, 222, 3, 193-199, doi:10.1016/s0048-9697(98)00305-2, 1998.

Tanaka, K., Takahashi, Y., Sakaguchi, A., Umeo, M., Hayakawa, S., Tanida, H., Saito, T. and Kanai, Y.: Vertical profiles of iodine-131 and cesium-137 in soils in Fukushima prefecture related to the Fukushima Daiichi Nuclear Power Station accident, Geochemical Journal, 46, 1, 73-76, doi:10.2343/geochemj.1.0137, 2012.

Tanoi, K., Nobori, T., Shiomi, S., Saito, T., Kobayashi, N. I., Leonhardt, N. and Nakanishi, T. M.: Chapter 3 Cesium Translocation in Rice, Agricultural Implications of the Fukushima Nuclear Accident (III), Springer, 15-25,2019.

Tarboton, D. G.: A new method for the determination of flow directions and upslope areas in grid digital elevation models, Water resources research, 33, 2, 309-319, doi:10.1029/96wr03137, 1997.

51

Tarboton, D. G.: Topographic Wetness Index, http://hydrology.usu.edu/taudem/taudem5/help53/TopographicWetnessIndex.html, Last Accessed: July 1, NA.

Tatsuno, T., Hamamoto, S., Nihei, N. and Nishimura, T.: Effects of the dissolved organic matter on Cs transport in the weathered granite soil, Journal of environmental management, 254, 109785, doi:10.1016/j.jenvman.2019.109785 2020.

Teramage, M. T., Onda, Y., Patin, J., Kato, H., Gomi, T. and Nam, S.: Vertical distribution of radiocesium in coniferous forest soil after the Fukushima nuclear power plant accident, Journal of environmental radioactivity, 137, 37-45, doi:10.1016/j.jenvrad.2014.06.017, 2014.

Tesfa, T. K., Tarboton, D. G., Chandler, D. G. and McNamara, J. P.: Modeling soil depth from topographic and land cover attributes, Water Resources Research, 45, 10, doi:10.1029/2008wr007474, 2009.

The Arms Control Association: The Nuclear Testing Tally https://www.armscontrol.org/factsheets/nucleartesttally, Last Accessed: June 25, 2019.

Tsoulfanidis, N.: Nuclear energy: selected entries from the encyclopedia of sustainability science and technology, Springer Science & Business Media, 2012.

Tsuda, T., Tokinobu, A., Yamamoto, E., & Suzukib, E.: Thyroid Cancer Detection by Ultrasound Among Residents Ages 18 Years and Younger in Fukushima, Japan: 2011 to 2014, Epidemiology, 20, 00-00, doi:10.1097/ede.0000000000000385, 2015.

Tsuji, H., Nishikiori, T., Yasutaka, T., Watanabe, M., Ito, S. and Hayashi, S.: Behavior of dissolved radiocesium in river water in a forested watershed in Fukushima Prefecture, Journal of Geophysical Research: Biogeosciences, 121, 10, 2588-2599, doi:10.1002/2016jg003428, 2016.

Tsukada, H., Hasegawa, H., Hisamatsu, S. i. and Yamasaki, S. i.: Transfer of 137 Cs and stable Cs from paddy soil to polished rice in Aomori, Japan, Journal of environmental radioactivity, 59, 3, 351-363, doi:10.1016/s0265-931x(01)00083-2, 2002.

Tukey, J. W.: Comparing individual means in the analysis of variance, Biometrics, 99-114, doi:10.2307/3001913, 1949.

Vanden Berghe, L. and Gulinck, H.: Fallout 137 Cs as a tracer for soil mobility in the landscape framework of the Belgian loamy region, Pedologie, 37, 1, 5-20, 1987.

Wakai, N., Yamashita, J., Enomoto, T., Tadashi, H., Ono, T. and Maeda, M.: Factors affecting 137Cs concentration in wild plants and soils of different land use in Iitate village after the Fukushima nuclear power plant accident, Radiation Safety Management, 18, 1-8, doi:10.12950/rsm.180918, 2019.

Wallbrink, P., Roddy, B. and Olley, J.: A tracer budget quantifying soil redistribution on hillslopes after forest harvesting, Catena, 47, 3, 179-201, doi:10.1016/s0341-8162(01)00185-0, 2002.

Walling, D., He, Q. and Quine, T.: Use of caesium-137 and lead-210 as tracers in soil erosion investigations, IAHS Publications-Series of Proceedings and Reports-Intern Assoc Hydrological Sciences, 229, 163-172, 1995.

Walling, D., Zhang, Y. and He, Q.: Models for converting measurements of environmental radionuclide inventories (137Cs, Excess 210Pb, and 7Be) to estimates of soil erosion and deposition rates (including software for model implementation), Department of Geography, University of Exeter, UK, 2007.

Wicherek, S. P. and Bernard, C.: Assessment of soil movements in a watershed from Cs-137 data and conventional measurements (example: the Parisian Basin), Catena, 25, 1-4, 141-151, doi:10.1016/0341-8162(95)00006-e, 1995.

Wood, S. N.: On p-values for smooth components of an extended generalized additive model, Biometrika, 100, 1, 221-228, doi:10.1093/biomet/ass048, 2012.

Wood, S. N.: Generalized additive models: an introduction with R, Chapman and Hall/CRC, 2017.

Wrixon, A. D., I. Barraclough, and M. J. Clark: RADIATION, PEOPLE AND THE ENVIRONMENT, 2004.

Xinbao, Z., Higgitt, D. and Walling, D.: A preliminary assessment of the potential for using caesium-137 to estimate rates of soil erosion in the Loess Plateau of China, Hydrological Sciences Journal, 35, 3, 243-252, doi:10.1080/02626669009492427, 1990.

Yang, C., Peterson, C., Shropshire, G. and Otawa, T.: Spatial variability of field topography and wheat yield in the palouse region of the Pacific Northwest, Transactions of the ASAE, 41, 1, 17, doi:10.13031/2013.17147, 1998.

Zaslavsky, D. and Sinai, G.: Surface hydrology: I—explanation of phenomena, Journal of the Hydraulics Division, 107, 1, 1-16, 1981.